**Atmospheric
Chemistry
and Physics**

Space-borne measurements of mesospheric magnesium species – a retrieval algorithm and preliminary profiles

M. Scharringhausen[1], A. C. Aikin[2], J. P. Burrows[1], and M. Sinnhuber[1]

[1]Institute of Environmental Physics, University of Bremen, Bremen, Germany
[2]Institute for Astrophysics and Computational Sciences, The Catholic University of America, Washington, D.C., USA

Abstract. We present a joint retrieval as well as first results for mesospheric air density and mesospheric Magnesium species (Mg and Mg^+) using limb data from the SCIAMACHY instrument on board the European ENVISAT satellite.

Metallic species like neutral Mg, ionized Mg^+ and others (Fe, Si, Li, etc.) ablate from meteoric dust, enter the gas phase and occur at high altitudes (≥ 70 km). Emissions from these species are clearly observed in the SCIAMACHY limb measurements. These emissions are used to retrieve total and thermospheric column densities as well as preliminary profiles of metallic species in the altitude range of 70–92 km. In this paper, neutral Magnesium as well as its ionized counterpart Mg^+ is considered. These species feature resonance fluorescence in the wavelength range 279 and 285 nm and thus have a rather simple excitation process.

A radiative transfer model (RTM) for the mesosphere has been developed and validated. Based on a ray tracing kernel, radiances in a large wavelength range from 240–300 nm covering limb as well as nadir geometry can be calculated. The forward model has been validated and shows good agreement with established models in the given wavelength range and a large altitude range.

The RTM has been coupled to a retrieval based on Optimal Estimation. Air density is retrieved from Rayleigh backscattered light. Mesospheric Mg and Mg^+ number densities are retrieved from their emission signals observed in the limb scans of SCIAMACHY. Other species like iron, silicon, OH and NO can be investigated in principle with the same algorithm. Based on the retrieval presented here, SCIAMACHY offers the opportunity to investigate mesospheric species on a global scale and with good vertical resolution for the first time.

1 Introduction

The major source for metal species in the upper atmosphere is assumed to be influx of meteoric particles and cosmic dust. These particles enter the atmosphere at high velocities (12–72 km/s) and evaporate in the middle and upper atmosphere due to frictional heating with the ambient air.

The altitude of evaporation depends on the evaporation temperature of the species considered here. More volatile compounds ablate at higher altitudes. Table 1 gives an overview of evaporation points and approximative altitude ranges of maximum ablation of some species. Additionally, the relative abundances by mass in cosmic dust are given (abridged from Plane, 2003).

The ionic counterparts of the neutral metal species are formed by either charge transfer with nitrogen or oxygen or one of the ionization processes described below (see Sect. 1.1).

At altitudes between 50 and 100 km and higher, the intensity of solar radiation in the UV is strong, and thus the atmosphere is partly ionized. Equally, this altitude region can be ionized by precipitating energetic particles from e.g. the sun. A major part of these particles is trapped within the radiation belts formed by the Earth's magnetic field and precipitate to lower altitudes near the auroral ovals or the polar caps.

1.1 Chemistry of Mg and Mg^+

This section gives a brief overview of the meospheric chemistry of the two Magnesium species considered in this study. In general, the following is true for all mesospheric metals: As a result of high ionization rate at high altitudes (above 90 km), the dominant reactions and processes including metal species are determined by ion chemistry. At lower altitudes, major species for reaction with metal species are O, O_2, O_3, H, H_2 and H_2O, and the metals will form stable oxides or hydroxides as their dominant compounds (Plane, 2003).
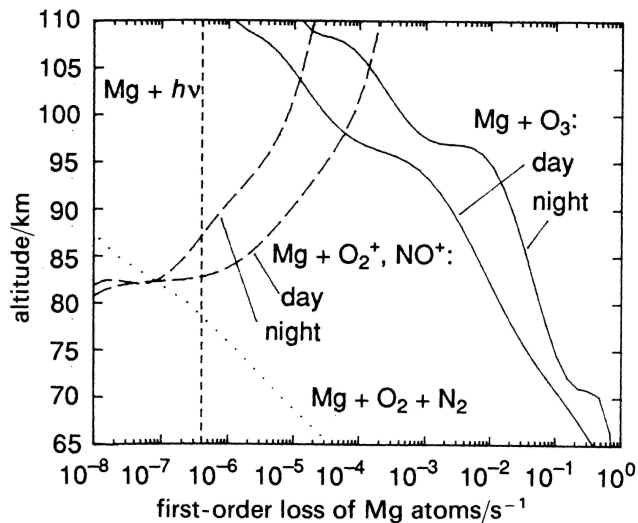
Fig. 1. Loss rates in the Earth's atmosphere (north mid-latitude winter scenario) for neutral Mg (adapted from Plane and Helmer, 1995).

Table 1. Features of meteoric metals. S: Species, EP: Evaporation point, MA: Maximal ablation, ARM: Average relative mass. Abridged from (Plane, 2003).

S	EP	MA	ARM
Mg	1363 K	80–90 km	12.5%
Fe	3023 K	?	11.5%
Na	1156 K	90–110 km	0.6%
Si	2628 K	?	?

Magnesium is the metal species of highest meteoric abundance. Though the ionized species Mg^+ has been measured occasionally by rocket-borne mass spectrometers, very little is known about the abundances of the neutral atom. This is mainly due to the fact that ground-based measurement techniques (lidar, photometry) using the Mg fundamental emission at 285 nm are impossible due to the strong ozone absorption in the Huggins bands at these wavelengths and lower altitudes.

Intense laboratory studies as well as model simulations have been undertaken (Plane and Helmer, 1995) to estimate loss and production processes at respective altitudes.

The major loss reactions under consideration are oxidation and ionization:

$$Mg + O_3 \rightarrow MgO + O_2 \tag{1}$$

$$Mg + O_2 + N_2 \rightarrow MgO_2 + N_2 \tag{2}$$

$$Mg + h\nu (\leq 162.2 \, nm) \rightarrow Mg^+ \tag{3}$$

$$Mg + NO^+ \rightarrow Mg^+ + NO \tag{4}$$
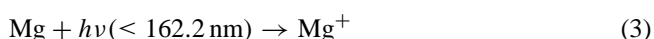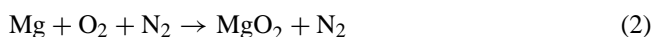
$$Mg + O_2^+ \rightarrow Mg^+ + O_2 \tag{5}$$

Figure 1 shows the first-order loss rates of neutral magnesium in different altitudes for a December mid-latitude scenario. Despite some diurnal variability the dominant loss process below 95 km is Eq. (1). Photoionization as well as Eq. (2) play a minor role. The diurnal variations are due to variations in the rate of photoionization (Eqs. 4, 5) and photolysis (Eq. 3).

Neutral Mg is mainly recovered by hydrogenolysis of a hydroxyl compound Eq. (8) as well as by oxidation of MgO Eq. (6). The ionic side of reaction pathways (Eqs. 9, 10) includes dissociative recombination of Mg^+ oxides Eqs. (11, 12):

$$MgO + O \rightarrow Mg + O_2 \tag{6}$$

$$MgO_2 + H \rightarrow MgOH + O \tag{7}$$

$$MgOH + H \rightarrow Mg + H_2O \tag{8}$$

$$Mg^+ + O_2 + M \rightarrow MgO_2^+ + M \tag{9}$$

$$Mg^+ + O_3 \rightarrow MgO^+ + O_2 \tag{10}$$

$$MgO^+ + e^- \rightarrow Mg + O \tag{11}$$

$$MgO_2^+ + e^- \rightarrow Mg + O_2 \tag{12}$$

The most stable neutral magnesium species is the dihydroxide $Mg(OH)_2$. It is formed by reaction of an Magnesium oxide with water Eq. (13). The only destruction reaction to matter in the upper atmosphere is reaction with atomic hydrogen (which leads to recovery of neutral Mg Eqs. (14, 8). Low number densities of atomic hydrogen on the one hand and increasing number densities of water vapour in lower altitudes on the other hand make $Mg(OH)_2$ a very efficient reservoir species for Mg.

$$MgO + H_2O + M \rightarrow Mg(OH)_2 + M \tag{13}$$

$$Mg(OH)_2 + H \rightarrow MgOH + H_2O \tag{14}$$
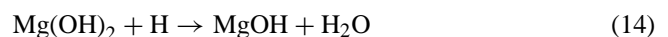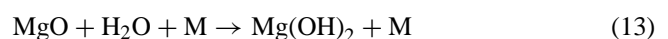
We use SCIAMACHY limb measurements in an altitude region of 70–92 km to simultaneously analyze Mg and Mg^+ profiles. Thus, the partitioning as well as the spatial variabilities of Mg and Mg^+ can be investigated.
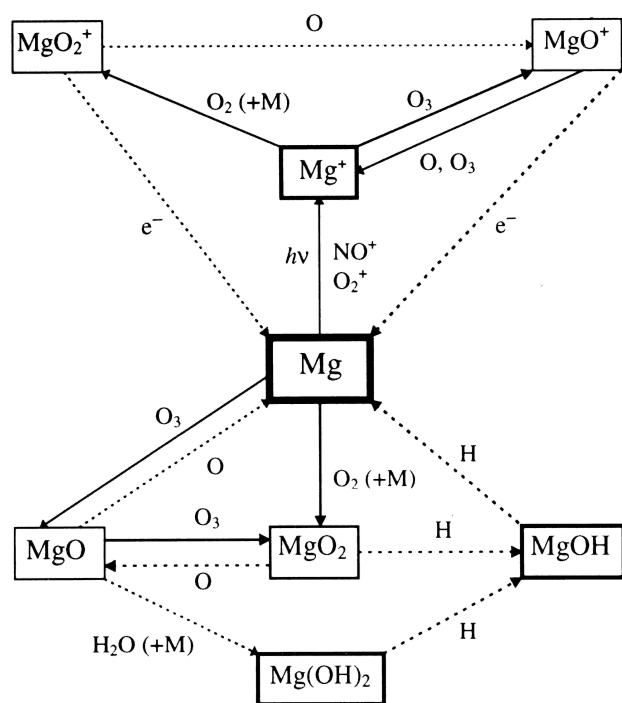
Fig. 2. Overview of the chemistry of Mg, Mg^+ and respective compounds in the upper atmosphere (Plane and Helmer, 1995).
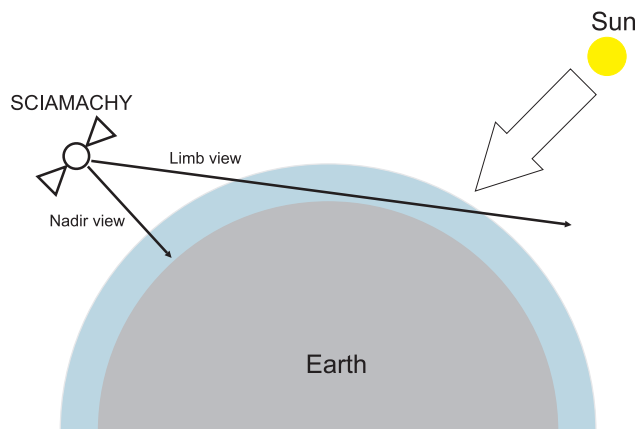

Fig. 3. SCIAMACHY viewing geometries. The occultation mode (looking directly into the sun) is not shown here). The limb viewing mode is used exclusively throughout the retrieval presented here.
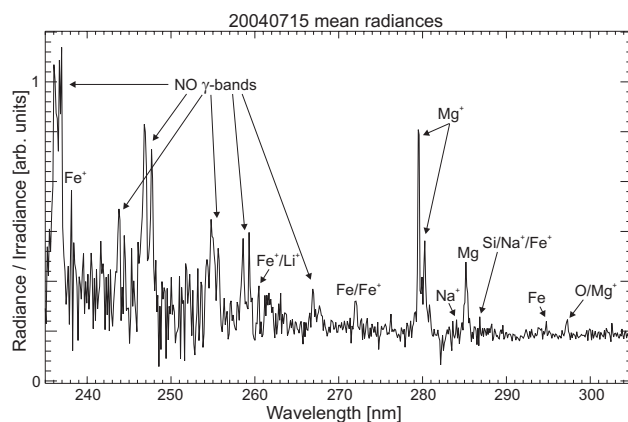

Fig. 4. Identified emission signals in SCIAMACHY channel 1. Shown is the ratio of radiances to solar irradiances of the same day taken by SCIAMACHY to emphasize several emission signals.

2 The SCIAMACHY instrument

The European ENVISAT satellite launched in March 2002 carries three instruments designed to perform observations of the atmosphere. Beside the Fourier transform spectrometer MIPAS and the stellar occultation device GOMOS, there is the SCIAMACHY instrument (**S**canning **I**maging **A**bsorption Spectro**m**eter for **A**tmospheric **Ch**artograph**y**).

SCIAMACHY covers the wavelength range from 220 to 2380 nm with a spectral resolution of 0.2 to 1.5 nm and provides nadir, limb and occultation viewing modes (Noel et al., 1999), see Fig. 3. The limb viewing mode covers altitude levels from 0 to 92 km. This altitude range covers a large part of the mesosphere. Limb scans are used to obtain altitude information of number densities, whereas the nadir mode provides total columns ranging from the ground to the exosphere.

The SCIAMACHY wavelength range includes emission signals of several metallic and non-metallic species (Fig. 4). Most emissions to be investigated in this study occur in the middle UV range. Beside emissions of the neutral species Fe, Mg and other the singly ionized forms of at least Fe and Mg can be observed as well. Additionally, the strong Na emission doublet at 589 nm can be observed easily in the SCIAMACHY spectra. Oxygen species like O, O_2, NO present some other prominent emission features in the UV-Vis-NIR wavelength region.

3 Retrieval method

3.1 The forward model

3.1.1 Measurement geometry

The SCIAMACHY instrument has three measurement modes (Sect. 2): limb, nadir and occultation. We consider only the limb viewing mode where the line-of-sight (LOS) is parallel to a tangent of the Earth's surface. Sunlight enters the atmosphere and gets scattered or absorbed. In case of absorption, radiation may be re-emitted e.g. by resonance fluorescence. The instrument detects all radiation that is scattered or emitted into the LOS (Fig. 5).
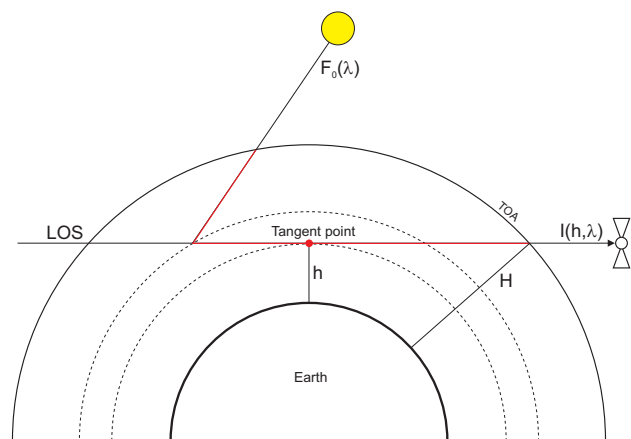
Fig. 5. The limb observational geometry of SCIAMACHY. This forward model covers tangent altitudes from $h=50$ km on upwards. Note however that due to strong absorption in the O_3 Hartley-Huggins bands, atmospheric information can be gained from limb UV measurements only above approx. 65 km, depending on the wavelength region under consideration. The top-of-atmosphere TOA is assumed to be at an altitude of $H=120$ km.

3.1.2 Basic assumptions

The SCIAMACHY instrument observes sunlight scattered and radiation emitted by the atmosphere. The number density of aerosols in the mesosphere is negligible and thus – apart from noctilucent clouds – only Rayleigh scattering is presumed. Since the following considerations are restricted to applications within a wavelength range of 240–300 nm, all extinction is assumed to be due to ozone absorption in the Hartley-Huggins bands and Rayleigh single scattering out of the line-of-sight.

As multiple scattering in general increases the path length within the atmosphere, the fraction of multiply scattered radiation transmitted to the instrument is very small due to the strong wavelength dependence of Rayleigh scattering and the large absorption cross sections of O_3 at wavelengths below 300 nm. Thus effects of multiple single scattering are neglected. The top-of-atmosphere is assumed to be at $H=120$ km for all solar zenith angles. That is, the model assumes no atmosphere above this altitude.

All emissions considered are assumed to be due to resonance fluorescence. Self absorption of the emitters is accounted for.

It is assumed that the atmosphere is homogeneous horizontally as well as vertically within a layer of thickness Δh. This value can be chosen by the user (see Sect. 3.4). It should be noted, however, that it is not clear how small scale structures influence the analysis.

Though radiation emitted due to resonance fluorescence is unpolarized, the polarization of Rayleigh scattering depends on the scattering angle. As SCIAMACHY consists of grid spectrometer devices, the radiation intensity detected

depends on the polarization of the light entering the instrument. This polarization sensitivity of the instrument is accounted for.

The radiative transfer model presented here will be denoted by MARS (**M**esospheric **A**tmospheric **R**adiative Transfer **S**imulator). It has been compared to the radiative transfer model SCIARAYS (see Kaiser, 2001). Results of limb calculations agree within 2.5% in an altitude range of 60–95 km, a wavelength range of 250–300 nm, and a range of the solar angles of 0–88 for zenith and 0–180 for azimuth.

3.1.3 Rayleigh scattering and ozone absorption cross sections

We use the Cabannes form (Chandrasekhar, 1960) of the Rayleigh scattering cross section for gaseous species. The following formula is slightly simplified according to the fact that the refractive index of the gaseous species under consideration is close to unity:

$$\varepsilon_{\text{Ray}}(\lambda) = \frac{32\pi^3(n_s-1)^2}{3\lambda^4 N_L^2} F_{\mathbf{K}}, \tag{15}$$

where the wavelength λ is given in nanometers, $N_L=2.69\cdot10^{19}$ cm^{-3} denotes the Loschmidt number, and $F_{\mathbf{K}}$ is the King correction factor:

$$F_{\mathbf{K}} = \frac{6+3\rho}{6-7\rho}. \tag{16}$$

Here, ρ is the depolarization factor of air. The commonly used value $\rho=0.0295$ (used e.g. in Rozanov, 2001) is used in this radiative transfer model. The refractive index of standard air n_s is calculated using the Edlén formula (Edlen, 1966):

$$n_s - 1 = (n_1 + n_2 + n_3) \cdot 10^{-8} \tag{17}$$

$$n_1 = 8342.13 \tag{18}$$

$$n_2 = \frac{2406030}{130 - 10^6\lambda^{-2}} \tag{19}$$

$$n_3 = \frac{15997}{38.9 - 10^6\lambda^{-2}} \tag{20}$$

$$n_s - 1 = \left(8342.13 + \frac{2406030}{130 - 10^6\lambda^{-2}} + \frac{15997}{38.9 - 10^6\lambda^{-2}}\right) \cdot 10^{-8} \tag{21}$$

The Rayleigh phase scattering function is given by

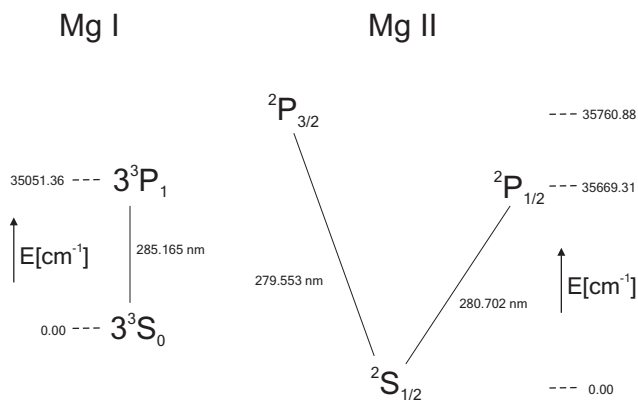$$P(\theta) = \frac{3}{2(2+\rho)}\left((1+\rho)+(1-\rho)\cos^2(\theta)\right), \tag{22}$$

Mg I

Mg II

$^2P_{3/2}$ --- 35760.88

35051.36 --- $3\,^3P_1$

$^2P_{1/2}$ --- 35669.31

$E[\text{cm}^{-1}]$ 285.165 nm

279.553 nm

280.702 nm $E[\text{cm}^{-1}]$

0.00 --- $3\,^3S_0$

$^2S_{1/2}$ --- 0.00

Fig. 6. Simplified Grotrian diagrams of Mg I and Mg II. Only the transitions used for the retrieval are shown.

where θ denotes the scattering angle (Eichmann, 1995). The probability of scattering into a solid angle $d\Omega$ under the scattering angle θ is given by $P(\theta)d\Omega/4\pi$.

Ozone absorption cross sections are taken from laboratory measurements (Burrows et al., 1999).

3.1.4 g-factors

The case of resonance fluorescence to the ground state is considered only. That is, the retrieval species are assumed to be excited by sunlight of wavelength λ_{ij} from the ground state i to an energetically upper state j. De-excitation then leads to unpolarized radiation of the same wavelength. Due to low number densities of all species considered here de-excitation by quenching is neglected. It should be noted, that the emitted radiation is in general not isotropic. See (Scharringhausen et al., 2007) and (Scharringhausen, 2007) for an extended version of the retrieval algorithm involving anisotropic emission.

The g-factor links number density and emitted radiance, e.g.

$$I_{ij} = \gamma_{ij} \cdot N \tag{23}$$

Quantities indexed with ij correspond to the transition from the upper state j to the lower state i. The g-factor is calculated as the product of the actinic flux, the absorption cross section σ_{ij} and the relative Einstein coefficient of spontaneous emission (Anderson and Barth, 1971). Here, σ_{ij} depends on the classical electron radius as well as on the transition wavelength λ_{ij} and the oscillator strength f_{ij}. The relative Einstein coefficient presents the probability of relaxation to the lower state i. Note that there may be a number of lower states reachable from state j. This is accounted for by normalising $\mathbf{A}_{ij}$ by the sum of all respective absolute Einstein coefficients.

$$\gamma_{ij} = \pi \, \boldsymbol{F}(\lambda_{ij}) \cdot \sigma_{ij} \cdot \frac{\mathbf{A}_{ij}}{\sum_{i'} \mathbf{A}_{i'j}} \tag{24}$$

$$= \pi \, \boldsymbol{F}(\lambda_{ij}) \cdot \frac{\pi e^2}{mc^2} f_{ij} \lambda_{ij}^2 \cdot \frac{\mathbf{A}_{ij}}{\sum_k \mathbf{A}_{kj}} \tag{25}$$

In the last equation, the factors present the actinic flux, the absolute cross section and the relative Einstein coefficient, respectively.

$$\gamma_{ij} = \pi \, \boldsymbol{F}(\lambda_{ij}) \cdot \sigma_{ij} \cdot \frac{\mathbf{A}_{ij}}{\sum_{i'} \mathbf{A}_{i'j}} \tag{26}$$

$$= \underbrace{\pi \, \boldsymbol{F}(\lambda_{ij})}_{\text{actinic flux}} \cdot \underbrace{\frac{\pi e^2}{mc^2} f_{ij} \lambda_{ij}^2}_{\text{abs. cross section}} \cdot \underbrace{\frac{\mathbf{A}_{ij}}{\sum_k \mathbf{A}_{kj}}}_{\text{rel. Einstein coeff.}} \tag{27}$$

All values necessary for numerical calculations are obtained from the NIST database (NIST, 2005).

3.1.5 Irradiance and radiance computations

The extinction of radiation traversing the atmosphere follows the Lambert-Beer-Law. The absorption coefficient $k(\boldsymbol{x}, \lambda)$ at a point $\boldsymbol{x}$ within the atmosphere depends on the scattering/absorption cross sections at wavelength λ as well as on the number densities of the scatterers/absorbers. Throughout this paper, the total number of species under consideration will be denoted by nspecies. All cross sections are assumed to be independent of the point of evaluation $\boldsymbol{x}$. In particular, the ozone cross sections are assumed to be independent of temperature. This leads to the following expression for the absorption coefficients k:

$$k(\boldsymbol{x}, \lambda) = \sum_{i=1}^{\text{nspecies}} \boldsymbol{N}_i(\boldsymbol{x}) \cdot \sigma_i(\lambda) \tag{28}$$

$$= \langle \boldsymbol{N}(\boldsymbol{x}), \sigma(\lambda) \rangle \tag{29}$$

$$k(\boldsymbol{x}, \lambda) = \sum_{i=1}^{\text{nspecies}} \boldsymbol{N}_i(\boldsymbol{x}) \cdot \sigma_i(\lambda) = \langle \boldsymbol{N}(\boldsymbol{x}), \sigma(\lambda) \rangle \tag{30}$$

Using the Lambert-Beer's law leads to the optical thickness τ_{sun}, τ_{sat} (indexed with sun respectively. sat to account for different light paths from the sun to the scattering point respectively. from the scattering point to the satellite). To calculate the solar irradiance $\boldsymbol{F}(Q, \lambda)$ present at a point Q within the atmosphere, it is necessary to integrate the absorption coefficient from Q to the TOA along the light path connecting the sun with Q:

$$\boldsymbol{F}(Q, \lambda) = \boldsymbol{F}_0(\lambda) \cdot \exp\left(-\int_Q^{\text{TOA}} k(s, \lambda) \, ds\right) \tag{31}$$

$$= \boldsymbol{F}_0(\lambda) \cdot \tau_{\text{sun}}(Q, \lambda) \tag{32}$$

A parameterization of the light path can be obtained by using the solar zenith and azimuth angle Φ, Ψ.

The conversion of irradiance $\boldsymbol{F}$ to radiance I is done by applying the Rayleigh phase function P and the emissivity respectively. the scattering cross section. As scattering and emission by resonance fluorescence are mathematically not distinguishable, the total emissivity can be written in a similar way as the absorption coefficient:

$$E(Q, \lambda) = \sum_{i=1}^{\text{nspecies}} \boldsymbol{N}_i(Q) \cdot \varepsilon_i(\lambda) \tag{33}$$

$$= \langle \boldsymbol{N}(Q), \varepsilon(\lambda) \rangle \tag{34}$$

$$E(Q, \lambda) = \sum_{i=1}^{\text{nspecies}} \boldsymbol{N}_i(Q) \cdot \varepsilon_i(\lambda) = \langle \boldsymbol{N}(Q), \varepsilon(\lambda) \rangle \tag{35}$$

Here, the quantity ε_i denotes the scattering cross section respectively the g-factor of species i. The vector $\varepsilon \in \mathbb{R}^{\text{nspecies}}$ merges these values. The scattering angle necessary for scattering into the LOS is then just the angle between the sun direction at Q and the LOS. It depends on the local solar zenith angle as well as on the local solar azimuth angle. Let the scattering angle be denoted by θ_Q. Note

$$\theta_Q = \theta_Q(\Phi, \Psi) \tag{36}$$

The light scattered in the LOS and entering the instrument is subject to extinction once again. The extinction between Q and the instrument can be calculated analogously:

$$\tau_{\text{sat}}(Q, \lambda) = \exp\left(-\int_Q^{+\text{TOA}} \langle \boldsymbol{N}(s), \sigma(\lambda) \rangle \, ds\right) \tag{37}$$

Here, $+$TOA denotes the top-of-atmosphere towards the satellite.

To obtain the total radiance at the instrument, the radiances at all points Q along the LOS have to be integrated and weighted with the respective optical thickness:

For a more convenient notation, set

$$P(s) = P(\theta_Q(s)) \tag{38}$$

$$E(s) = E(Q(s), \lambda) \tag{39}$$

$$\tau_{\text{sun}}(s, \lambda) = \tau_{\text{sun}}(Q(s), \lambda) \tag{40}$$

$$\tau_{\text{sat}}(s, \lambda) = \tau_{\text{sat}}(Q(s), \lambda) \tag{41}$$

Then the following equation for the total limb radiance holds:

$$I(\lambda) = \boldsymbol{F}_0(\lambda) \cdot \int_{-\text{TOA}}^{+\text{TOA}} J(s) \, ds \tag{42}$$

$$J(s) = \tau_{\text{sun}}(s, \lambda) \cdot E(s, \lambda) \cdot P(s) \cdot \tau_{\text{sat}}(s, \lambda) \tag{43}$$

$$I(\lambda) = \boldsymbol{F}_0(\lambda) \cdot \int_{-\text{TOA}}^{+\text{TOA}} \tau_{\text{sun}}(Q(s), \lambda) \cdot E(Q(s), \lambda) \cdot$$
$$P(\theta_Q(s)) \cdot \tau_{\text{sat}}(Q(s), \lambda) \, ds \tag{44}$$

$$= \boldsymbol{F}_0(\lambda) \cdot \int_{-\text{TOA}}^{+\text{TOA}} \tau_{\text{sun}}(s, \lambda) \cdot E(s, \lambda) \cdot P(s) \cdot \tau_{\text{sat}}(s, \lambda) \, ds \tag{45}$$

Here, $Q(s)$ denotes a parametrization of the LOS, and $-$TOA corresponds to the TOA away from the satellite. The second equation is a more convenient form of the first.

These integrals are evaluated by numerical quadrature using an adaptive grid (see Sect. 3.4). That is, the atmosphere is divided into altitude layers and all quantities are evaluated at discrete locations along the respective light paths. The trapezoid rule is used throughout the retrieval, as it is simple, fast and accurate at the same time.

Let $n_{\text{sun}}, n_{\text{sat}}, n_{\text{LOS}}$ be the number of points the light paths are divided into. The $c_{\text{sun},i}, c_{\text{sat},i}, c_{\text{LOS},i}$ denote air mass factors (AMF) along the light paths, the discrete correspondences of the differential operators ds:

$$c_{*,i} = s_{i+1} - s_i \tag{46}$$

The following equations for the absorption coefficients and the total radiance hold:

$$\tau_{\text{sun}}(Q, \lambda) = \exp\left(-\sum_{i=1}^{n_{\text{sun}}+1} \alpha_{\text{sun},i}\right)$$
$$\alpha_{\text{sun},i} = \langle \boldsymbol{N}(s_i), \sigma(\lambda) \rangle c_{\text{sun},i} \tag{47}$$

$$\tau_{\text{sat}}(Q, \lambda) = \exp\left(-\sum_{i=1}^{n_{\text{sat}}+1} \alpha_{\text{sat},i}\right)$$
$$\alpha_{\text{sat},i} = \langle \boldsymbol{N}(s_i), \sigma(\lambda) \rangle c_{\text{sat},i} \tag{48}$$

$$I(\lambda) = \boldsymbol{F}_0(\lambda) \cdot \sum_{i=1}^{n_{LOS}} J_i$$

$$J_i = \tau_{sun}(s_i, \lambda) E(s_i, \lambda) P(s_i) \cdot \tau_{sat}(s_i, \lambda) c_{LOS,i}$$

$$\tau_{sun}(Q, \lambda) = \exp\left(-\sum_{i=1}^{n_{sun}+1} \langle N(s_i), \sigma(\lambda)\rangle c_{sun,i}\right)$$

$$\tau_{sat}(Q, \lambda) = \exp\left(-\sum_{i=1}^{n_{sat}+1} \langle N(s_i), \sigma(\lambda)\rangle c_{sat,}\right)$$

$$I(\lambda) = \boldsymbol{F}_0(\lambda) \cdot \sum_{i=1}^{n_{LOS}} \tau_{sun}(s_i,\lambda) \cdot E(s_i,\lambda) \cdot$$

$$P(s_i) \cdot \tau_{sat}(s_i, \lambda) \cdot c_{LOS,i} \tag{49}$$

3.1.6 Instrument simulator for limb geometry

In limb mode, the SCIAMACHY instrument performs 31 to 35 limb scans from the surface to $\approx$92 km tangent altitude in steps of approx. 3.3 km. A last measurement is taken at 150–200 km, which is not included into the forward model. The instrument has a vertical field-of-view (FOV) of 2.6 km. Thus, the instrument convolves all radiation within the FOV. This is accounted for by calculating the radiance on a fine altitude grid (stepsize 1 km) and then convolving the values with the SCIA FOV slit function of full-width-half-maximum (FWHM) W=2.6 km.

For this purpose two slit functions have been tested.
Rectangular:

$$\mathbf{S}(h) = \begin{cases} 0 & , |h| \geq W/2 \\ 1/W & , \text{else} \end{cases} \tag{50}$$

Gaussian, order 10:

$$\mathbf{S}(h) = \frac{1}{.9883\,W} \exp\left[-\left(\frac{2\ln(2)\cdot h}{W}\right)^{10}\right] \tag{51}$$

The standardization constant for the Gaussian is found using the following method: The integral $\int_{-\infty}^{\infty} S(h)dh$ is evaluated for a number of values for $1 \leq \boldsymbol{F} \leq 10$. The relationship between $\boldsymbol{F}$ and the value of the integral is virtually linear, and the integral vanishes for $\boldsymbol{F}$=0. The regression coefficient is found to be between 1.068 and .9941, and the relative error is well below .5% for all values of $\boldsymbol{F}$. This method has been tested for Gaussians of order 2…20.

Differences between the results using different slit functions are found to be small and thus a Gaussian of order 10 is used throughout all calculations.

3.2 The retrieval

3.2.1 Basic principles

Taking into account nalt altitude levels and nlam wavelengths, the observed limb radiances can be joined together in a measurement vector y. The same holds for the number density profiles of all species (remember that nspecies denotes the total number of species), these are merged in an atmospheric state vector $\boldsymbol{x}$:

$$y \in \mathbb{R}^{\text{nlam} \cdot \text{nalt}} \quad , \quad \boldsymbol{x} \in \mathbb{R}^{\text{nspecies} \cdot \text{nalt}} \tag{52}$$

The forward computations are treated in an analogous way using a discrete forward model operator $\boldsymbol{F}$ that depends on the atmospheric state $\boldsymbol{x}$:

$$\boldsymbol{F} : \mathbb{R}^{\text{nspecies} \cdot \text{nalt}} \longrightarrow \mathbb{R}^{\text{nlam} \cdot \text{nalt}} \tag{53}$$

However, due to discretization and other effects such as uncertainties in measuring the observational parameters (SZA, altitude, etc) one has to allow for a forward error δ:

$$y = \boldsymbol{F}(\boldsymbol{x}) + \delta \tag{54}$$

The aim of the retrieval is to invert $\boldsymbol{F}$ to find $\boldsymbol{x}$. However, this problem is ill-posed, e.g. due to noise in the measurement it cannot be assumed that y (or $y - \delta$) lies within the range of $\boldsymbol{F}$. That is, in general, Eq. (54) has no exact solution. Moreover, the altitude resolution is limited as one limb view traverses the entire atmosphere. All altitudes above (and, due to the finite width of the field-of-view, to a certain extend even below) the tangent altitude contribute to the observed radiance. The latter is true even for a ideal measurement with no noise. Thus, the best one can do is to minimize

$$||y - \boldsymbol{F}(\boldsymbol{x})||^2_{\mathbf{S_y^{-1}}}, \tag{55}$$

where $\mathbf{S_y}$ denotes the measurement covariance matrix. This way, knowledge about the measurement uncertainties can be introduced as weighting factors in the retrieval. However, in general there is an infinite number of atmospheric state vectors $\boldsymbol{x}$ that minimize Eq. (55). Additionally, small perturbations of y due to noise may lead to large variations of the retrieval result. This may lead to large oscillations.

Thus, some kind of regularization has to be applied to restrict space of possible solutions. The most common regularization scheme is the Tikhonov regularization using a priori information $\boldsymbol{x}_a$:

$$||y - \boldsymbol{F}(\boldsymbol{x})||^2_{\mathbf{S_y^{-1}}} + ||\boldsymbol{x} - \boldsymbol{x}_a||^2_{\mathbf{S_a^{-1}}} \to \min \tag{56}$$

Here, $\mathbf{S_a}$ presents the a priori covariance matrix. This matrix contains a priori uncertainties of the atmospheric parameters. This approach has been adapted and reformulated by Rodgers (see Rodgers, 1976) to derive the Optimal Estimation method.

3.2.2 Weighting functions

The derivations of the limb radiances with respect to the atmospheric state parameters x_j constitute the weighting function matrix $\mathbf{K}$:

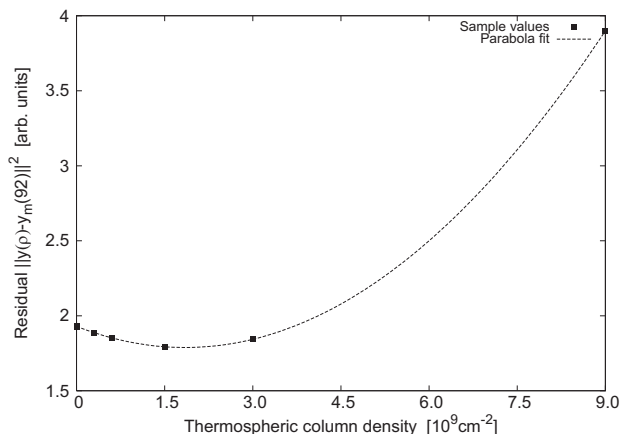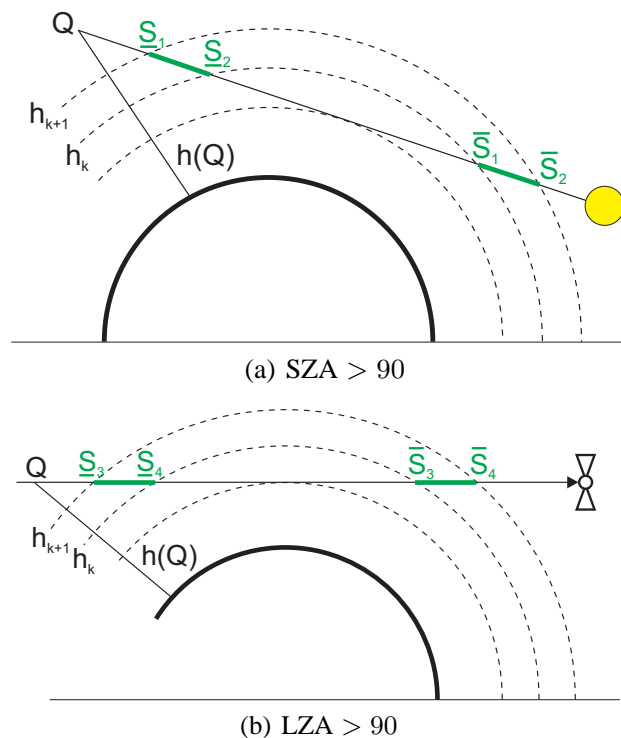$$\mathbf{K}_{ij} = \frac{\partial F_i}{\partial x_j} \tag{57}$$

Fig. 7. AMF to be used in the calculations of the weighting functions. A number of cases with respect to the solar zenith angle (SZA) an the LOS-zenith-angle (LZA) have to be distinguished.

(a) SZA > 90

(b) LZA > 90

Fig. 8. AMF to be used in the calculations of the weighting functions. A number of cases with respect to the solar zenith angle (SZA) an the LOS-zenith-angle (LZA) have to be distinguished.

For simplicity, we consider only a single species. Let N_j be the number density of the species within the altitude layer $[h_j, h_{j+1}]$. To compute the derivations of the optical thicknesses, a number of cases have to be distinguished in terms of the solar zenith angle (SZA) and the LOS zenith angle (LZA) (see Figs. 7, 8):

$$\frac{\partial \tau_{sun}(Q, \lambda)}{\partial N_j} = \frac{\partial}{\partial N_j} \exp(-\alpha) \tag{58}$$

LZA $\leq$ 90:

$$\alpha = \int_{s_1}^{s_2} N(s)\sigma(\lambda)\,ds \tag{59}$$

LZA > 90:

$$\alpha = \int_{\underline{s}_1}^{\underline{s}_2} N(s)\sigma(\lambda)\,ds - \int_{\overline{s}_1}^{\overline{s}_2} N(s)\sigma(\lambda)\,ds \tag{60}$$

LZA $\leq$ 90:

$$\frac{\partial \tau_{sun}(Q, \lambda)}{\partial N_j} = \frac{\partial}{\partial N_j} \exp\left(-\int_{s_1}^{s_2} N(s)\cdot\sigma(\lambda)\,ds\right) \tag{61}$$

LZA > 90:

$$\frac{\partial \tau_{sun}(Q, \lambda)}{\partial N_j} = \frac{\partial}{\partial N_j} \exp$$
$$\left(-\int_{\underline{s}_1}^{\underline{s}_2} N(s)\cdot\sigma(\lambda)\,ds - \int_{\overline{s}_1}^{\overline{s}_2} N(s)\cdot\sigma(\lambda)\,ds\right) \tag{62}$$

$$\frac{\partial \tau_{sat}(Q, \lambda)}{\partial N_j} = \frac{\partial}{\partial N_j} \exp(-\alpha) \tag{63}$$

SZA $\leq$ 90:

$$\alpha = \int_{s_3}^{s_4} N(s)\sigma(\lambda)\,ds \tag{64}$$

SZA > 90:

$$\alpha = \int_{\underline{s}_3}^{\underline{s}_4} N(s)\sigma(\lambda)\,ds - \int_{\overline{s}_3}^{\overline{s}_4} N(s)\sigma(\lambda)\,ds \tag{65}$$

SZA $\leq$ 90:

$$\frac{\partial \tau_{sat}(Q, \lambda)}{\partial N_j} = \frac{\partial}{\partial N_j} \exp\left(-\int_{s_3}^{s_4} N(s)\cdot\sigma(\lambda)\,ds\right) \tag{66}$$

SZA > 90:

$$\frac{\partial \tau_{sat}(Q, \lambda)}{\partial N_j} = \frac{\partial}{\partial N_j}$$
$$\exp\left(-\int_{\underline{s}_3}^{\underline{s}_4} N(s)\cdot\sigma(\lambda)\,ds - \int_{\overline{s}_3}^{\overline{s}_4} N(s)\cdot\sigma(\lambda)\,ds\right) \tag{67}$$

Note that if $h_{j+1} < h(Q)$, the integrals vanish.

$$\frac{\partial E(Q, \lambda)}{\partial N_j} = \begin{cases} \varepsilon(\lambda), & h_j \leq h(Q) \leq h_{j+1} \\ 0, & \text{else} \end{cases} \tag{68}$$

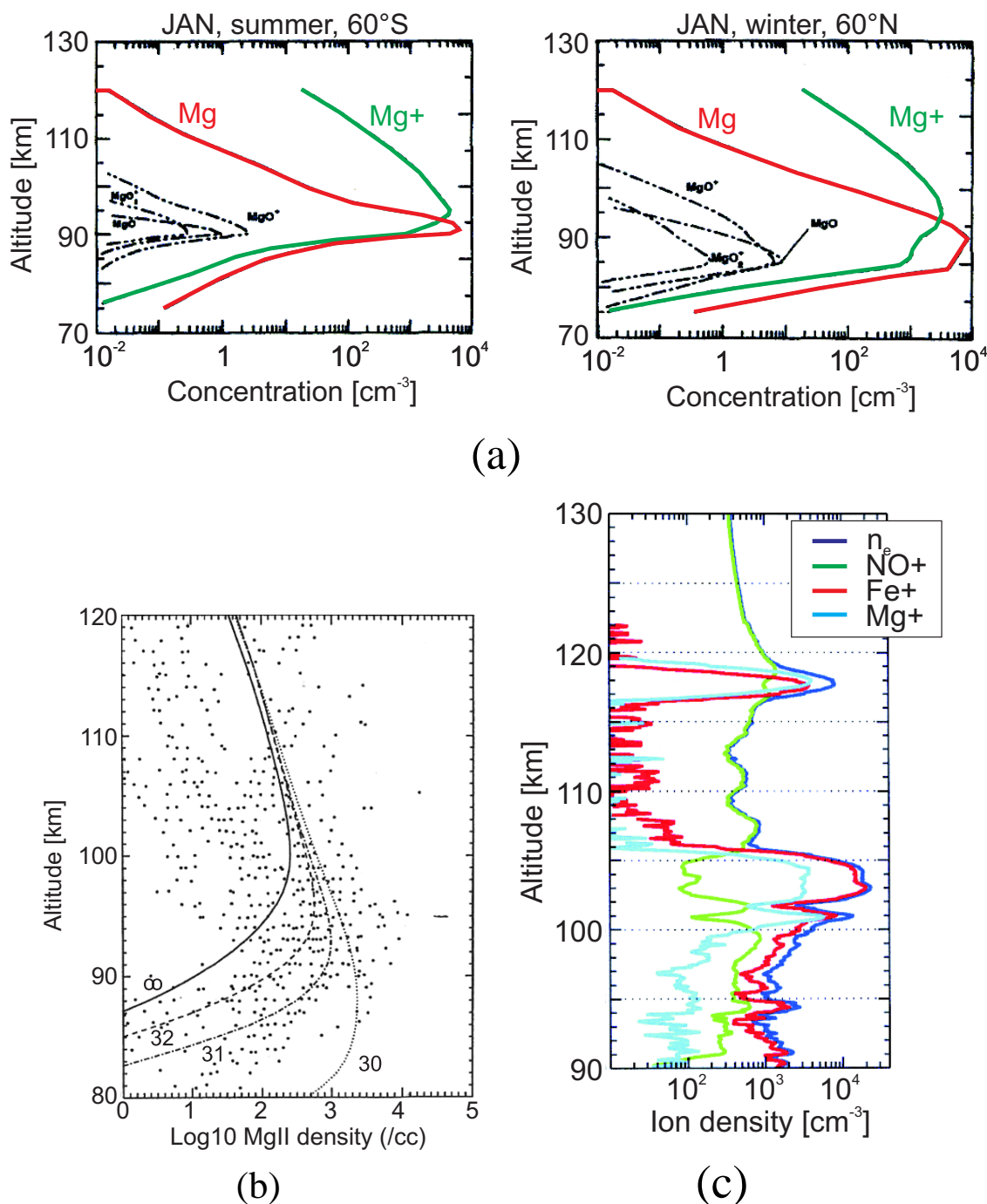The derivative of the radiance at a certain tangent altitude is calculated using the above formulas:

(a)

(b)

(c)

Fig. 9. Overview of model calculations (a,b,c) and rocket sounding measurements (c,d) of Magnesium species. **(a)**: Vertical distribution of ionized and neutral Mg for January noon condition at 50 southern (a) respectively. northern **(b)** latitude. Abridged from (Fritzenwallner and Kopp, 1998). Maximum MgI and MgII abundances are predicted between 90 and 100 km. **(c)**: Comparison of the MgII layer predicted by model calculations, taken from (McNeil et al., 1998). The four curves correspond to different rate constants r (given in $cm^{-6}s^{-1}$) for the reaction $Mg^+ + 2N_2 \rightarrow MgN_2^+ + N_2$. Curves are denoted by $-\ln(r)$. Scattered: Ion mass spectrometry measurements published in Grebowsky et al., 1998. These measurements suggest highest abundances of MgII to occur at altitudes above 90 and below 105 km. Model calculations predict a layer with maximum abundance at altitudes between 87 and 105 km, depending on r. **(d)**: Ion composition data observed by rocket-borne ion mass spectrometry. Two distinct layers of MgII at 100–105 km and 116–119 km are observed. From (Roddy et al., 2004).
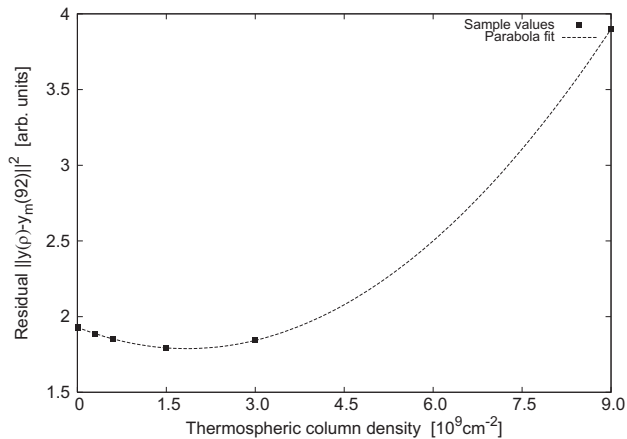
Fig. 10. Estimation of the thermospheric content. Six radiative transfer calculations with different sample values of the column density ρ_C are shown. Note that as the emission signal depends linearly on the thermospheric content, the residual $||y(\rho) - y_m(92)||^2$ can be described in a very good approximation as a parabola. The location of its minimum gives an estimation of the true ρ_C. Here, $\rho_C \approx 1.7 \cdot 10^9$ cm^{-2}.

$$
\begin{aligned}
\frac{\partial I(\lambda)}{\partial N_j} &= \frac{\partial}{\partial N_j} F_0 \cdot \int_{-\text{TOA}}^{+\text{TOA}} \tau_{\text{sun}} \cdot E \cdot P \cdot \tau_{\text{sat}} ds \\
&= F_0(\lambda) \cdot \int_{-\text{TOA}}^{+\text{TOA}} \left[\frac{\partial}{\partial N_j} \tau_{\text{sun}} \cdot E \cdot P \cdot \tau_{\text{sat}} \right. \\
&\quad + \tau_{\text{sun}} \cdot \frac{\partial}{\partial N_j} E \cdot P \cdot \tau_{\text{sat}} \\
&\quad + \left. \tau_{\text{sun}} \cdot E \cdot P \cdot \frac{\partial}{\partial N_j} \tau_{\text{sat}} \right] ds
\end{aligned}
\tag{69}
$$

These integrals are evaluated using quadrature algorithms as well.

3.2.3 Minimization method

The functional Eq. (56) is minimized using a Levenberg-Marquardt-style algorithm. Set

$$
G(x) = ||F(x) - y||^2_{\mathbf{S_y}^{-1}} + ||x - x_a||^2_{\mathbf{S_a}^{-1}}
\tag{70}
$$

The gradient and the Hessian of G are computed as follows:

$$
\nabla G(x) = \mathbf{K}^T \mathbf{S_y}^{-1}(F(x) - y) + \mathbf{S_a}^{-1}(x - x_a)
\tag{71}
$$

$$
\nabla^2 G(x) = \mathbf{K}^T \mathbf{S_y}^{-1} \mathbf{K} + \mathbf{S_a}^{-1}
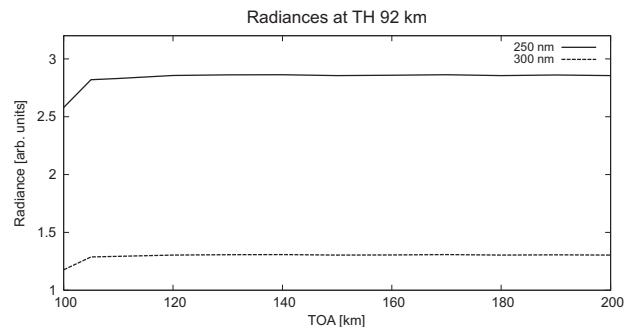\tag{72}
$$

Fig. 11. Radiances at 92 km for different values of TOA as calculated by the radiative transfer model. The relative differences are well below 1% for TOA's larger than 120 km.

A newton step consists of the solution of a linear system of equations:

$$
\nabla^2 G(x)\Delta x = -\nabla G(x)
\tag{73}
$$

$$
x \to x + x\Delta x
\tag{74}
$$

Unfortunately, the newton algorithm converges only locally and only in case the Hessian is positive definite. An algorithm with global but slow convergence is the method of gradient descent. This method uses the unit matrix $\mathbf{I}$ instead of the Hessian. Thus, the update step is

$$
x \to x - x\nabla G(x)
\tag{75}
$$

To overcome the disadvantages of both methods, the retrieval implemented here uses the Levenberg-Marquardt method, i.e. doing step like Eq. (73) using a dynamic convex combination of the unit matrix and the Hessian instead of the Hessian alone. If the Hessian is positive definite, Eq. (73) is performed. If the Hessian fails to be positive definite, the algorithm performs

$$
x \to x + x\Delta x , \quad B\Delta x = -\nabla G(x)
\tag{76}
$$

using

$$
B = (1 - \theta)\nabla^2 G(x) + \theta I
\tag{77}
$$

$$
\theta \in \{0., 0.1, 0.2, \ldots, 0.9, 1.\}
\tag{78}
$$

The parameter θ is chosen minimal such that B is positive definite. Different stepsizes in θ are possible.

The iterations may be stopped at a point $x^* \in x \in \mathbb{R}^{\text{nspecies} \cdot \text{nalt}}$ if one of the following criteria is fulfilled:

– The norm of $\nabla G(x)$ falls below a certain (relative) threshold (e.g. one percent of the initial norm).

– The residual $||\boldsymbol{F}(\boldsymbol{x}) - y||$ is below the noise.

– The residual $||\boldsymbol{F}(\boldsymbol{x}) - y||$ does not improve significantly in a certain set of successive iterations.

– The value $||\boldsymbol{x} - \boldsymbol{x_a}||$ does not change significantly in a certain set of successive iterations.

3.2.4 Error analysis

The method of Optimal Estimation does not provide an exact result, but rather a probability density function (PDF) of the true state of the atmosphere. This PDF is assumed to be of Gaussian shape, and the retrieval solution x_R actually constitutes the mean value. The covariance matrix can be written as follows:

$$\mathbf{S} = (\mathbf{K}^T \mathbf{S_y}^{-1} \mathbf{K} + \mathbf{S_a}^{-1})^{-1} \tag{79}$$

The diagonal values of this matrix are the variances σ_i^2 of the state vector elements x_i^*, and hence the standard deviations σ_i can be used as an estimation of the retrieval error. Throughout this paper, these values are used as estimations of the profile errors.

Let x_t be the true state of the atmosphere. Useful information is contained in the averaging kernel matrix

$$\mathbf{A} = \frac{\partial x^*}{\partial x_t}$$
$$= (\mathbf{K}^T \mathbf{S_y}^{-1} \mathbf{K} + \mathbf{S_a}^{-1})^{-1} \mathbf{K}^T \mathbf{S_y}^{-1} \mathbf{K} \tag{80}$$

$$\mathbf{A} = \frac{\partial \mathbf{x}^*}{\partial \mathbf{x}_t} = (\mathbf{K}^T \mathbf{S_y}^{-1} \mathbf{K} + \mathbf{S_a}^{-1})^{-1} \mathbf{K}^T \mathbf{S_y}^{-1} \mathbf{K} \tag{81}$$

This derivative reflects the influence of the true state on the retrieved one. An ideal measurement and retrieval would result in an unity matrix $\mathbf{A}$. As a real instrument like a limb sounder has a limited spatial resolution, the retrieved number density at an altitude $h(k)$ may be influenced by number density at lower and higher altitudes. This is quantified by the off-diagonal elements of the k-th row of $\mathbf{A}$. The vertical resolution can thus be estimated as the full-width-half-maximum (FWHM) of the averaging kernel function (which is discretely represented by the k-th row of $\mathbf{A}$) for this altitude.

Moreover, the sum of the k-th row of $\mathbf{A}$ can be used as an estimation of the measurement response. When it is close to 1, the retrieval result is completely determined by the measurement and not by the a priori.

The measurements of Mg and Mg$^+$ presented here exhibit very poor averaging kernels (see. Figs. 26, 28). However, this is just due to the fact that the a priori itself contains much information from the measurement due to the preconditioning (see Sect. 3.4.6).

3.3 Thermospheric content

Model calculations as well as rocket soundings (Plane and Helmer, 1995, Fritzenwallner and Kopp, 1998, McNeil et al., 1998, Roddy et al., 2004) indicate the highest number densities of metallic species at altitudes at or above the top tangent height of SCIAMACHY (92 km), see Fig. 9.

However, as a inherent feature of limb geometry, information about higher tangent altitudes is contained in every tangent altitude covered by SCIAMACHY. To gain information about the thermospheric content, the topmost limb scan is treated as a quasi-nadir measurement of the thermosphere. Self-absorption is very weak (however, it is accounted for in the retrieval) and absorption by scattering out of the LOS as well as absorption by O_3 is negligible at these high altitudes. Thus the signal of a certain emission species at 92 km depends almost linearly on the column density of this species (see Fig. 10).

The one-dimensional Newton method is used to estimate the thermospheric content. Let $y(\rho)$ be the forward computation vector corresponding to a thermospheric content ρ (given e.g. in cm^{-2}). The measurement at 92 km tangent altitude may be denoted $y_m(92)$. The minimum ρ_T of the function $\boldsymbol{F}(\rho) = ||y(\rho) - y_m(92)||^2$ then gives a good estimation of the thermospheric content.

3.4 Numerical issues

Though the general approach of discretization and numerical quadrature will lead to results in principle, the retrieval has to be designed to deal with a fundamental computational issue. That is, all calculations have to be done fast and accurate at the same time. To fulfill this need the following optimization steps have been applied:

3.4.1 Choice of TOA

The forward modelled radiance at high altitudes depends on the choice of the TOA - higher values of TOA will result in higher radiances. Although this is true for arbitrarily high TOA, the change in radiances tends to zero as the TOA increases. It has been found that radiances at all wavelengths within the range considered here increase less than 1% when changing the TOA from 110 to 120 km. Thus, a TOA of 120 km is chosen throughout the whole radiative transfer code.

3.4.2 Adaptive quadrature grids

The accuracy of the numerical quadrature depends crucily on the number and position of the quadrature points.

First, the LOS is divided in more parts if the tangent altitude decreases. The length of the LOS within the atmosphere varies from more than 1000 km at low tangent altitudes of 55–60 km to about 200 km at the topmost tangent height 92 km. This is accounted for. The lower the tangent altitude the more often the RTE is evaluated.
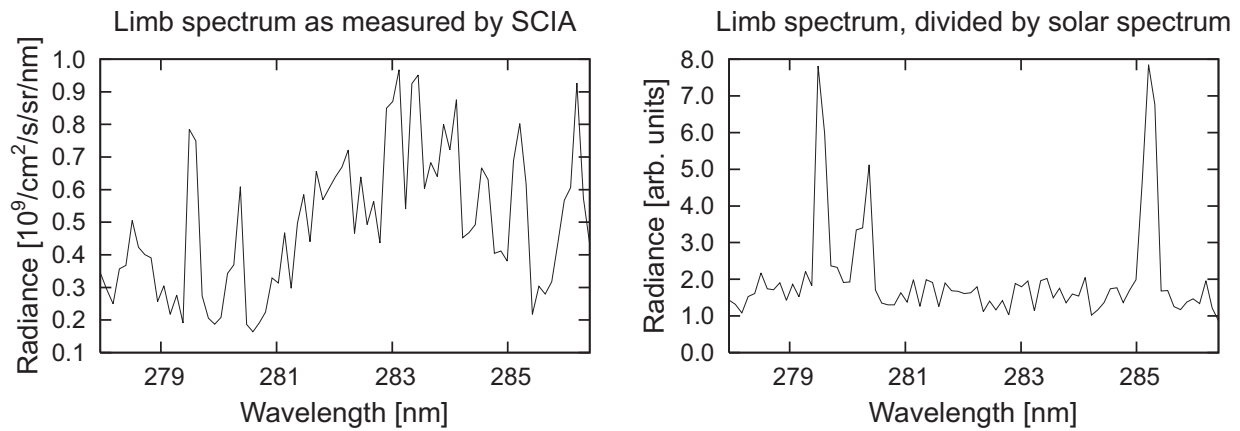
Limb spectrum as measured by SCIA

Limb spectrum, divided by solar spectrum

Fig. 12. The measured spectrum (left) is divided by a sun spectrum measured by SCIA to improve S/N (right). The emission features at 279.553/280.270 nm (MgII) and 285.213 nm (MgI) can be identified much more clearly in the right-hand spectrum.
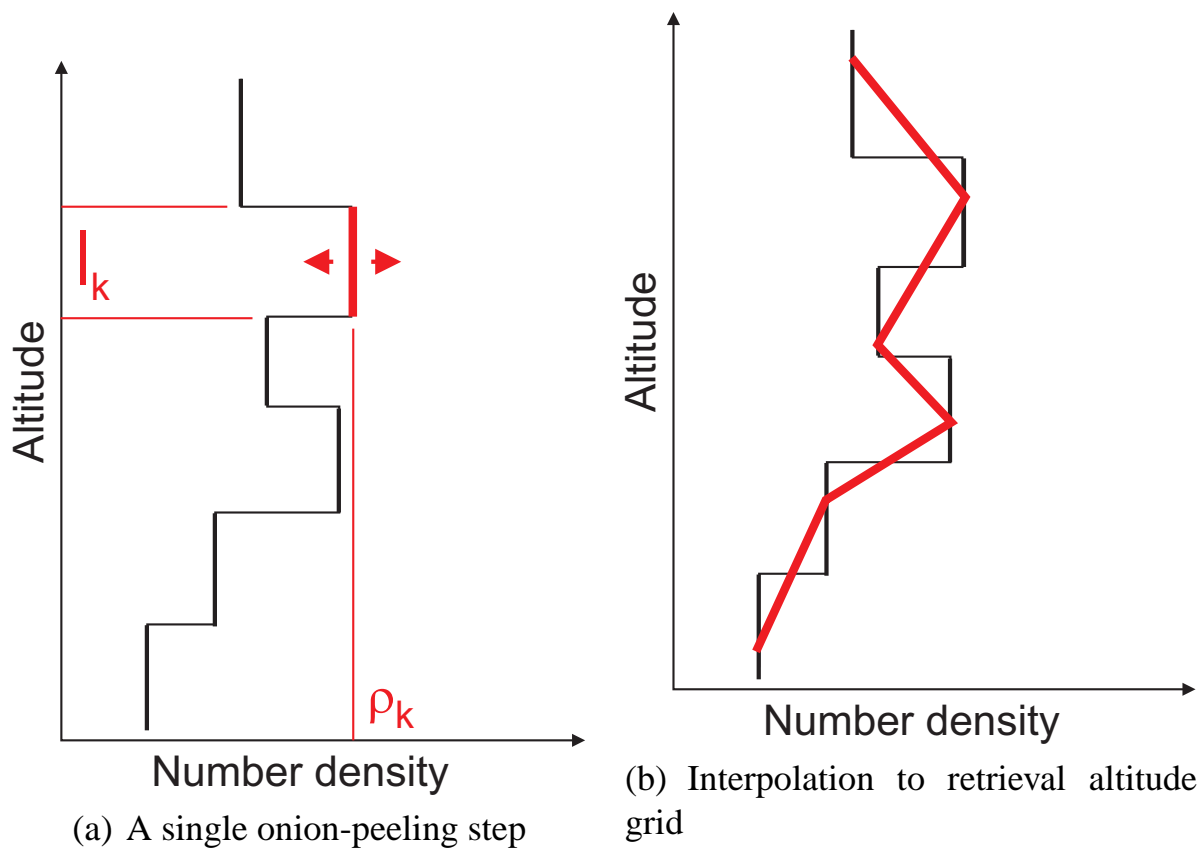
(a) A single onion-peeling step

(b) Interpolation to retrieval altitude grid

Fig. 13. Sketch of the onion-peeling method used as preconditioning step. Only one number density profile is shown. **(a)**: Fit forward model to measurement assuming number densities within altitude interval A_k to be constant. This is an one-dimensional problem. **(b)**: Interpolate the piecewise constant number densities on the fine altitude grid to the retrieval grid to obtain an a priori profile for the full optimal estimation retrieval.

Second, the traverse length of a sun-bound ray increases if the SZA increases. At 30 SZA the way a ray has to travel is about 70% less than at 60 SZA. Changing from 60 to 80, the path length increases by a factor of more than 2. This is accounted for. The higher the SZA, the more quadrature points are chosen along a ray.
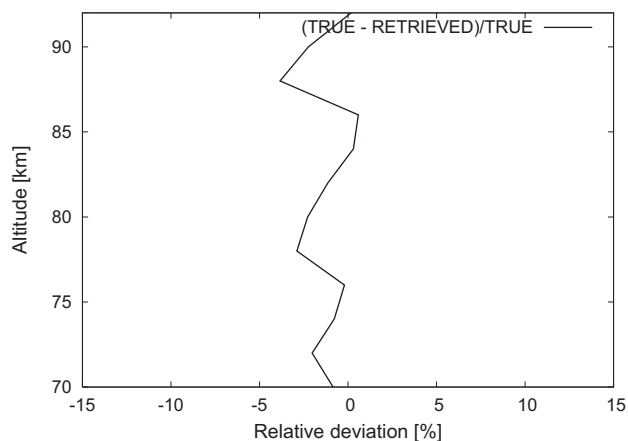
Fig. 14. Relative deviations of the retrieved from the true profile, SZA=60, SAA=30. Absolute values of the errors stay within ±4%.
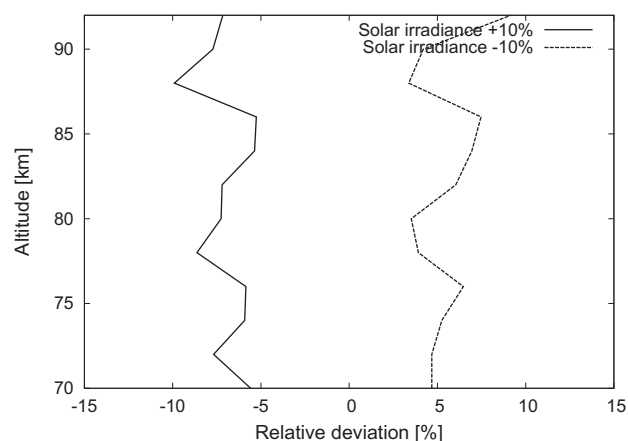
Fig. 15. Relative deviations from the true profile if the solar irradiance is changed by ±10%. The absolute values of the deviations stay within 5–10% over the altitude range 70–90 km.
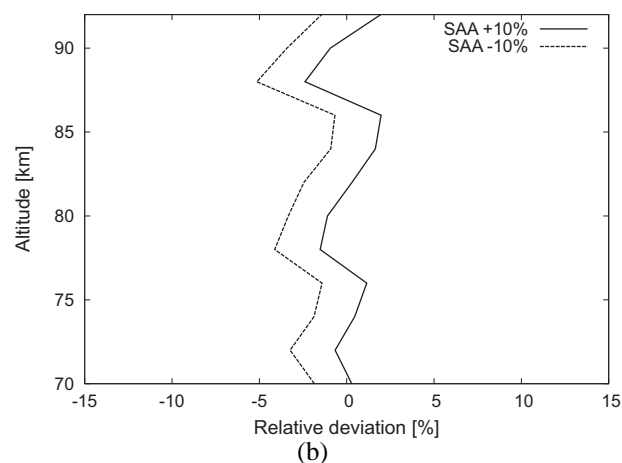

Fig. 16. (a): Relative deviations from the true profile if the solar zenith angle (SZA) of 60 is changed by ±10%. Absolute values lie between 0 and 6% error. **(b):** Relative deviations from the true profile if the solar azimuth angle (SAA) of 30 is changed by ±10%. Absolute values lie between 0 and 5%.

3.4.3 Separation of retrieval for different species

Rayleigh backscatter is a broadband effect. Line emissions, however, only feature observable signals at very few isolated wavelengths. Moreover, the backscatter radiances at wavelengths different from the emission/excitation wavelengths are not correlated with the emissions itself. A two-step retrieval has been developed to exploit this fact.

In a first step, the air and O_3 densities are determined from backscatter radiances near the emission wavelength. It is assumed that instrumental errors such as calibration behave similar for nearby wavelengths. Thus one may assume that a good background fit obtained from the first retrieval step will stay good when the wavelengths under consideration are changed a little bit for the second retrieval. The second retrieval then treats air and O_3 density as fixed while the number densities of the emission species are determined. These
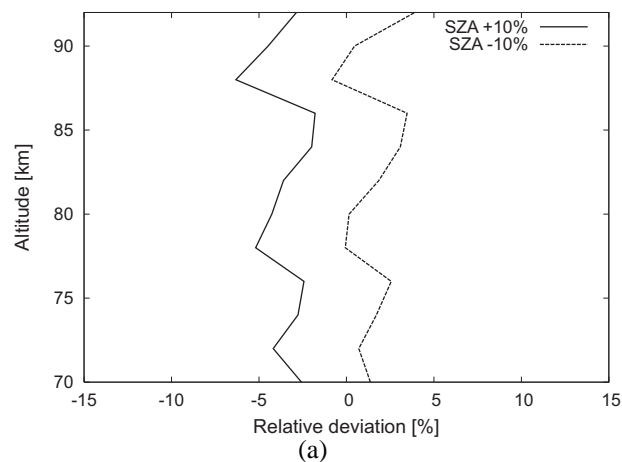
two steps provide a more reliable separation of the background radiance from the emission than using a fixed profile of air and O_3 for the retrieval of the emission species.

3.4.4 Relative deviations instead of absolute values

The radiative impact of the various species involved in the retrieval is highly variable. For example, the number density of mesospheric ozone is roughly six orders of magnitude smaller than the air density within the same altitude region. Though the absorption cross section of O_3 is larger than the Rayleigh scattering cross section of air, the absorption coefficients differ by up to four orders of magnitude, depending on the wavelength region.

To make computations more homogeneous and comparable, the estimated retrieval parameters (i.e. the atmospheric state vector) are not the number densities of the atmospheric
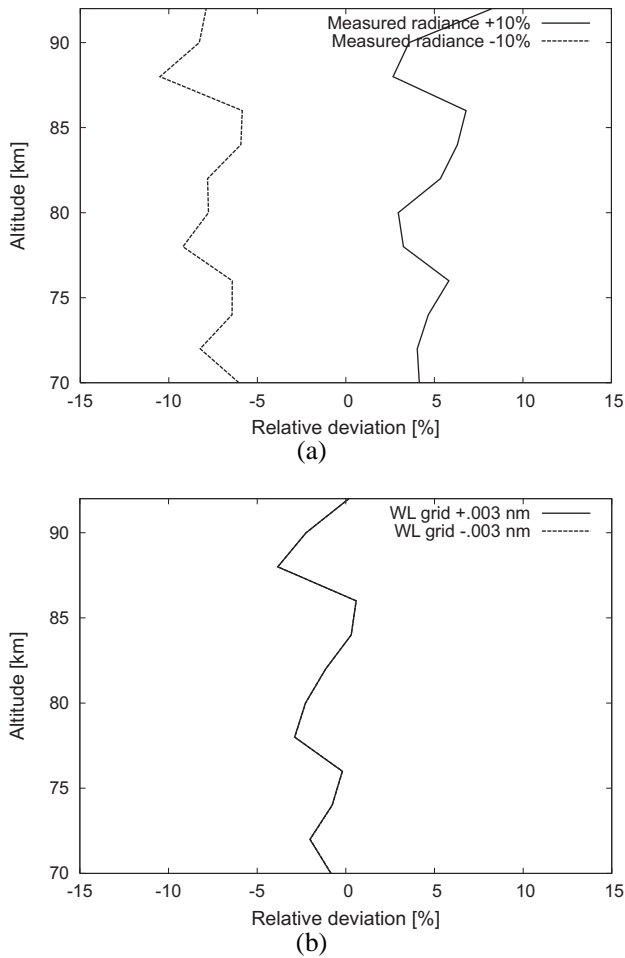
(a)

(a)

(b)

(b)

Fig. 17. **(c)**: Relative deviations from the true profile if the measured radiance is changed by ±10%. The retrieved profile deviates 2–10% from the true profile. **(d)**: Relative deviations from the true profile if wavelength grid is changed by ±.003 nm. This does not show any effect on the retrieved profile. Note that the two curves for +.003 nm and –.003 nm lie on top of each other.

Fig. 18. **(e)**: Relative deviations from the true profile if the absorption cross section of O_3 and air (the latter is identical to the Rayleigh scattering cross section) (SIGMA) are changed by ±10%. As the impact of absorption on the scattered light is decreasing with altitude, the relative deviations from the true profile increase at lower altitudes. However, absolute values stay well within ± 5%. **(f)**: Relative deviations from the true profile if the scattering cross section of air (EPSILON) ±10%. Absolute values stay well within ±10%.

species itself but rather their deviations from a respective given a priori profile. That is,

$$x = x^a + x^\delta \qquad (82)$$

where the actual retrieval result is given by

$$\frac{x^\delta}{x} = \begin{pmatrix} x_1^\delta/x_1 \\ \vdots \\ x_{\text{nspecies·nalt}}^\delta/x_{\text{nspecies·nalt}} \end{pmatrix} \qquad (83)$$

The usual first order Taylor series expansion for the forward model operator F

$$F(x + \Delta x) \approx F(x) + K \cdot \Delta x \qquad (84)$$

resp. $\quad \Delta y_i \approx \sum_j K_{ij} \Delta x_j \qquad (85)$

thus can be rewritten in the following manner:

$$\frac{F(x + \Delta x) - F(x)}{F(x)} \approx \widetilde{K} \cdot \frac{\Delta x}{x} \qquad (86)$$

resp. $\quad \dfrac{\Delta y_i}{y_i} \approx \sum_j \widetilde{K}_{ij} \dfrac{\Delta x_j}{x_j}, \qquad (87)$

where $\widetilde{K}$ is given by

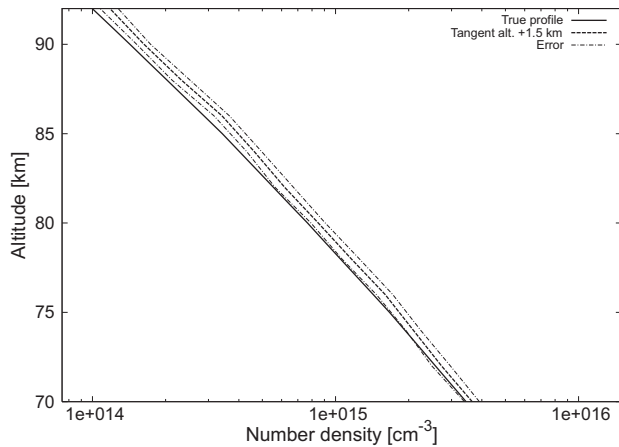$$\widetilde{K}_{ij} = K_{ij} \cdot \frac{x_j}{y_i} \qquad (88)$$

Fig. 19. The tangent height grid of the measurement is shifted by 1.5 km upwards. The plot shows the retrieved (dashed) and the true (solid) profile. The offset between the retrieved and the true profile is $\approx$.75 km within the altitude range 70–92 km.

According to this notation, $\widetilde{\mathbf{K}}_{ij}$ denotes the fractional variation of the radiances with respect to to the fractional variation of the atmospheric parameters.

3.4.5 Improvement of S/N

The emission signals are very small and heavily contaminated by noise. To get a more distinct signal, the measured spectrum is divided through by a solar spectrum (see Fig. 12). To prevent artefacts that are due to the different wavelength scales of the limb and the sun spectrum, the wavelength grid of the latter is adjusted to the grid of the first using a shift-and-squeeze algorithm. Note that calcibration issues of the detectors cancel out as a result of the division. The major difference between the measurement of the solar spectrum and the limb spectrum is the different optical pathway of the incident light, see (Noel et al., 1999). The latter publication estimates the relative error in the solar spectrum to be smaller than 5%.

3.4.6 Preconditioning by onion-peeling

Though the Levenberg-Marquardt is at least in theory a globally converging algorithm, it is desirable to provide an initial state vector x that is as good as possible. Starting with no information and using an arbitrarily chosen initial state vector x (e.g. a zero profile) may result in slow convergence or large oscillations of the number density profiles. The latter is due to the fact that several local minima of the retrieval functional Eq. (5) (Sect. 2.3) may be located very close to each other.

This is particularly true for the retrieval of the emission species Mg and Mg$^+$, since the signal is very weak in comparison to the measurement noise (S/N $\lesssim$ 2).
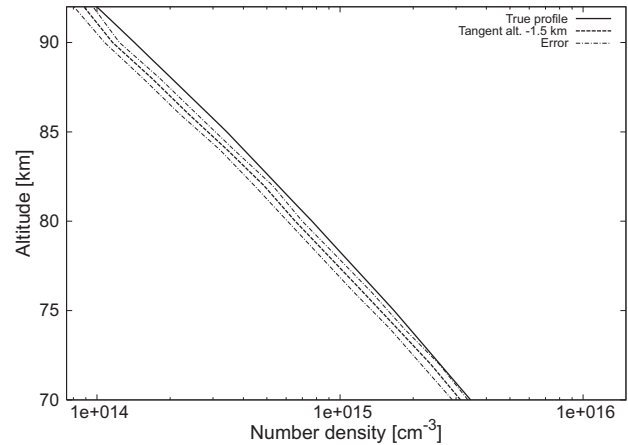

Fig. 20. The tangent height grid of the measurement is shifted by 1.5 km downwards. The plot shows the retrieved (dashed) and the true (solid) profile. The offset between the retrieved and the true profile is $\approx$.75 km within the altitude range 70–92 km.
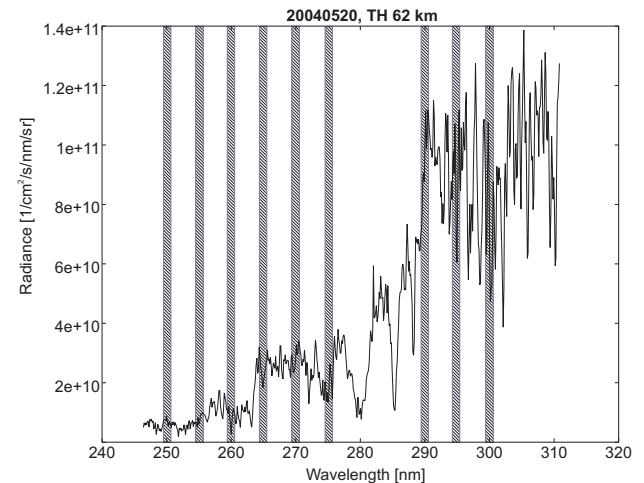

Fig. 21. Wavelength windows in SCIAMACHY channel 1 used for the retrieval of mesospheric air density. Each windows consists of four to five pixels to reduce the impact of noise on the retrieval. The positions of the wavelength bands are chosen avoiding atmospheric emission features.

To obtain a preliminary estimate of the number density at each tangent height, an onion-peeling method is used as a first step. It uses similar, multiply times applied method as the thermospheric estimation (Sect. 3). After determination of the thermospheric content, the following steps are performed for each tangent altitude $H(k)$ from the top tangent height on downward. Note that for each species these steps have to be performed likewise.

1. Consider the altitude interval

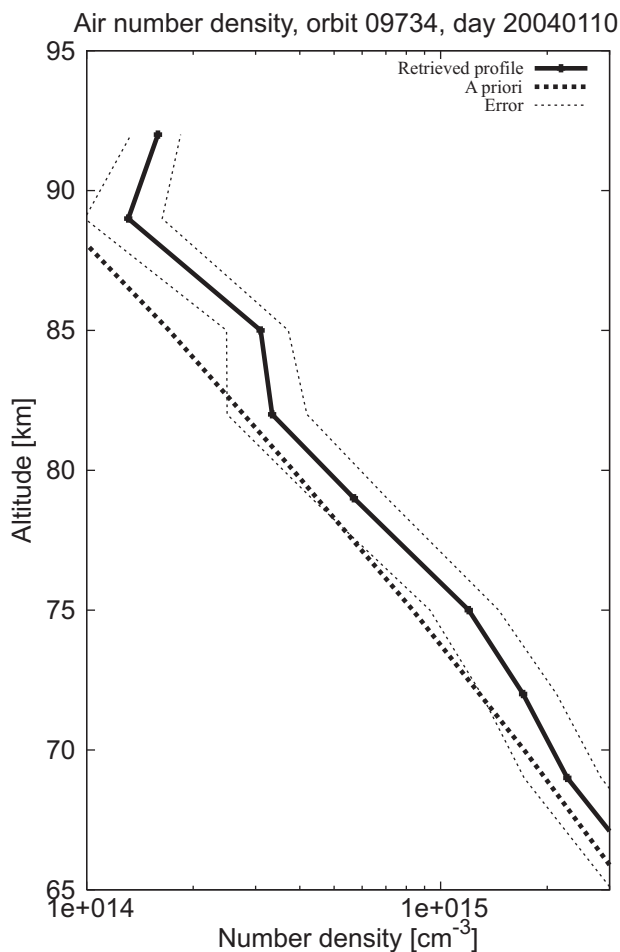$$\mathbf{A}_k := \left[\overline{H}_k, \overline{H}_{k+1} \right], \tag{89}$$

Fig. 22. Sample air density profile, as retrieved from orbit 09734, limb scan no. 10, 10 January 2004. Increased values above 85 km are due to straylight.
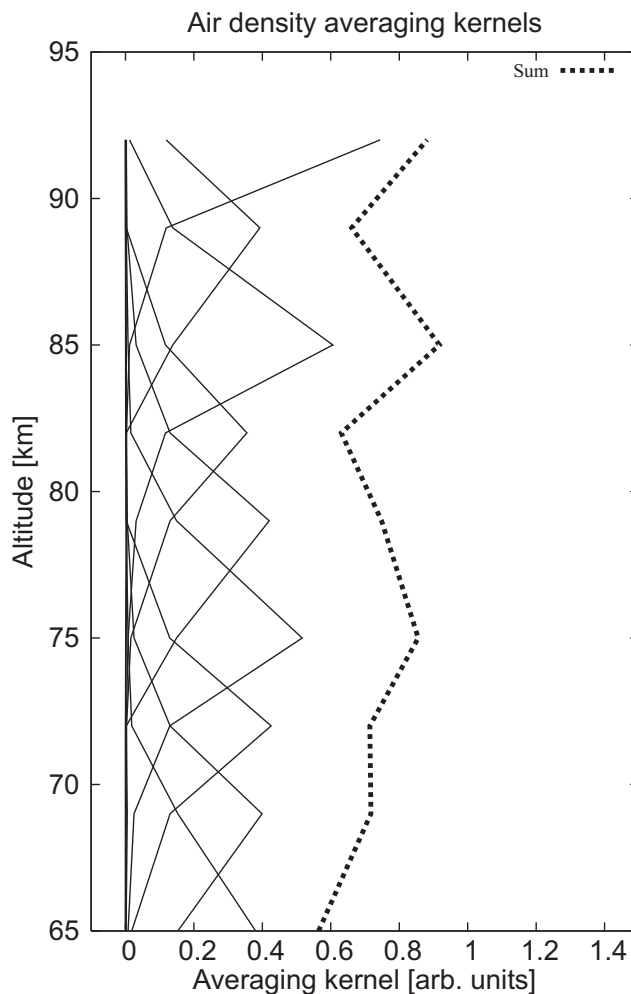

Fig. 23. Corresponding averaging kernels for air density (Fig. 22). The dashed line shows the sum of all kernels. Values near unity indicate that the profile is determined virtually exclusively by the measurement and not by the a priori. The FWHM of the kernel functions give a hint of the instrument's altitude resolution. It is approximately 5 km.

$$\overline{H}_k = \frac{H(k-1) + H(k)}{2} \tag{90}$$

$$\mathbf{A}_k := \left[\frac{H(k-1) + H(k)}{2}, \frac{H(k) + H(k+1)}{2} \right], \tag{91}$$

centered around tangent altitude $H(k)$. Keep all number densities at higher altitudes fixed.

2. Assume number densities to be equal at all altitudes within $\mathbf{A}_k$ (assign the name ρ, say, to this value. See Fig. 13) and minimize the functional

$$\boldsymbol{F}(\rho) = ||y(\rho) - y_m(k)||^2 + \gamma ||\rho - \rho_0||^2 \tag{92}$$

Here, $y_m(k)$ denotes the measurement at tangent altitude k and $y(\rho)$ denotes the modelled radiances that

are obtained by convolution over $\mathbf{A}_k$, assuming all number densities to have equal value ρ. The regularization factor γ may be interpreted as a one-dimensional covariance matrix $\mathbf{S_a}$ in a classical optimal estimation retrieval. It prevents the profile from suffering from large oscillations. The a priori value ρ_0 may take any value mirroring a priori knowledge. Here, $\rho_0{=}0$ is chosen.

Note that in case the radiative transfer is fairly linear, the above functional is well approximated by a parabola, any optimization method such as Newton's method or Regula falsi (the latter is chosen here due to computational time reasons) will do well.

The number density profiles with respect to the fine altitude grid are obviously piecewise constant. Interpolation to the
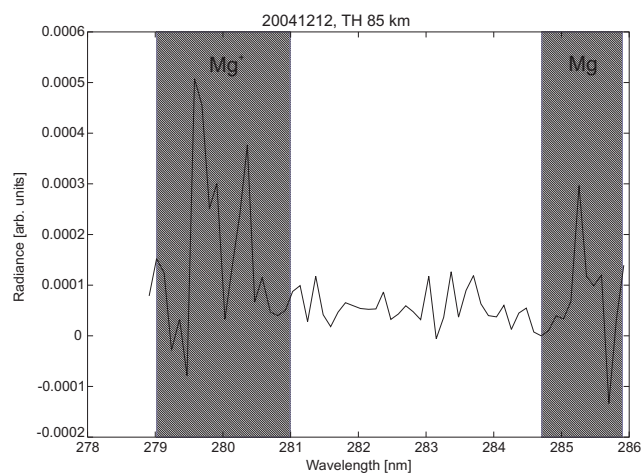
Fig. 24. Emission signals and wavelength windows in SCIA-MACHY channel 1 used for the retrieval of Mg and Mg^+ number densities. Note that the SCIAMACHY radiance is divided by a solar spectrum of the same day, as measured by SCIAMACHY. This way, the emission features can be observed more clearly.

retrieval grid then delivers profiles that are used as new initial profiles for the conventional optimal estimation retrieval (Fig. 13).

3.5 Sensitivity analysis

A number of retrieval runs have been performed to analyse the dependency and stability of the retrieved profiles with respect to the input parameters (absorption/scattering cross sections) as well as the measured data (irradiances, radiances, wavelength grid, SZA, SAA, tangent altitude grid). As a typical setup of SCIAMACHY measurements, the following parameters have been chosen to produce a synthetic measurement:

1. SZA=60, SAA=30

2. ACE model profiles of air density and O_3 density

3. Measurement noise 20%

The retrieval is run with the following setup:

1. Wavelength grid: three wavelength bins of 10 pixel each, situated at 250–251 nm, 270–271 nm, 295–296 nm. Similar results have been obtained using eight wavelength bins located between 250–300 nm (see Sect. 4.1).

2. Initial profile guess: true profile increased by 25%

3. Tangent altitudes: 70–92 km

At first, the retrieval was run without artificial errors on the parameters and measured data. The true profile as reproduced by the retrieval is very good. The absolute values of
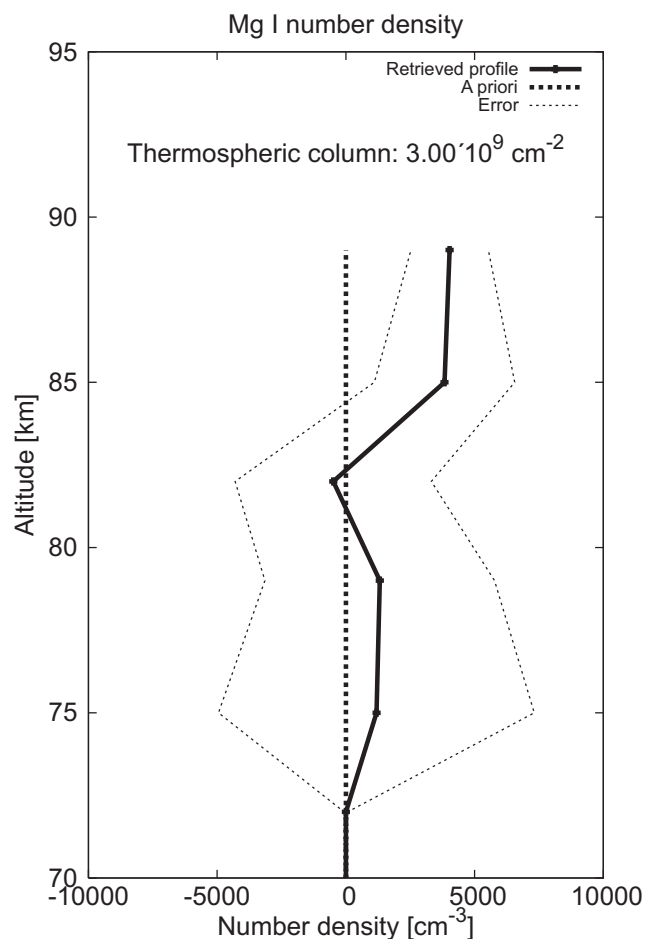

Fig. 25. Sample Mg density profile, as retrieved from orbit 09734, limb scan no. 10, 10 January 2004. Mg density is highest between 85 and 90 km. This agrees well with model calculations (Fig. 9).

the deviations are less than 4% (see Fig. 14). In terms of an artificial measurement noise of 20 %, this is a very good value.

It has been observed that the retrieval is error-decreasing. That is, introduction of artificial errors of a certain size results in retrieval errors of smaller size.

In detail, the following errors have been considered:

– An error of ±10% in the solar angles (zenith and azimuth). This is approximately the standard deviation when averaging all angles (zenith and azimuth, respectively) over one state, i.e. one limb scan from the bottom to the top. This error propagates through the retrieval to end up with a profile error of 6% or less (Fig. 16).

– An error in the measured radiance of ±10% (Fig. 17). This value is estimated from pre-flight design analysis (Bovensmann et al.).
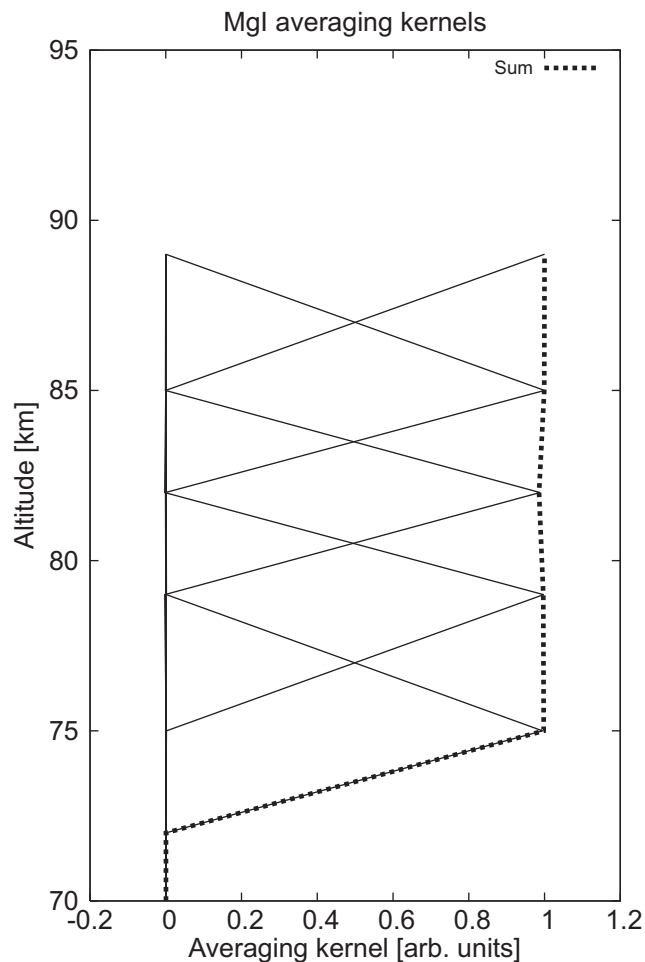
MgI averaging kernels

Fig. 26. Corresponding averaging kernels for Mg (Fig. 25). The dashed line shows the sum of all kernels. The profile is determined by the measurement within the altitude region 72–92 km. The FWHM of the kernel functions give a hint of the instrument's altitude resolution. It is approximately 5 km.

Mg II number density

Fig. 27. Sample Mg$^+$ density profile, as retrieved from orbit 09734, limb scan no. 10, latitude 22N, 10 January 2004. Column densities agree well with LIDAR observations (comp. Fritzenwallner and Kopp, 1998).

– A wavelength stability of $\pm.003$ nm has been estimated by (Bovensmann et al., 1999). This error has virtually no effect on the retrieved profiles (Fig. 17).

– The absorption cross sections have been perturbed by $\pm10\%$. This value accounts well for the temperature-dependency the absorption cross section of ozone as well as for the relative errors in laboratory determination of these values (Burrows et al., 1999). This perturbation shows increasing effect at lower altitudes (Fig. 18). This is quite reasonable, as the absorption has a minor contribution to the limb scattered radiance at high altitudes.

– The scattering cross sections have been perturbed by $\pm10\%$. This value has been chosen according to that of the absorption cross sections. Relative deviations from
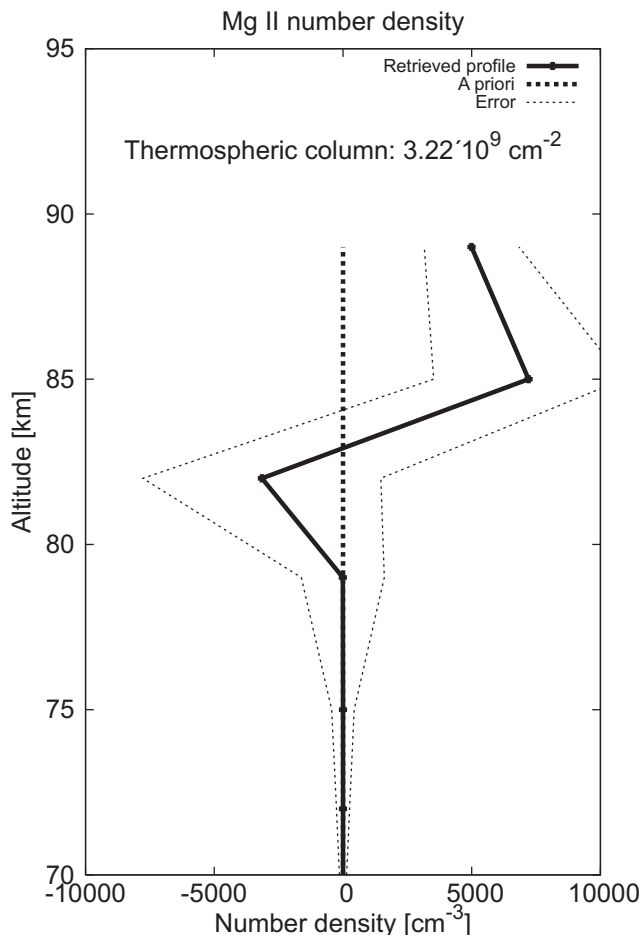
the true profile are altitude independent, but stay well within $\pm10\%$ (Fig. 18).

– Special attendance has been paid to the well-known pointing problem of SCIAMACHY (see Figs. 19, 20). The tangent heights of SCIAMACHY are known to be wrong by up to 1.5 km (v. Savigny et al., 2006). For completeness, a downshift is considered as well as an upshift by 1.5 km. The tangent height grid of the synthetic measurement is decreased respectively increased by 1.5 km and the retrieved profile is compared to the true profile. Surprisingly at first sight, the offset between the retrieved and the true profile has the same sign but is approximately half the offset of the respective tangent height grids. This may be due to the limited height resolution of SCIAMACHY, which is found to be approximately 5 km (twice the value of the tangent height step), see Sect. 4.1.

4 Results

4.1 Mesospheric air density

4.1.1 Retrieval settings

Mesospheric air density is retrieved from Rayleigh backscattered radiance.

As Rayleigh scattering is highly wavelength dependent, the retrieval is supposed to obtain information from a very large wavelength range. However, computational capacity and time limits restrict the coverable range. To overcome these disadvantages, a number of microwindows consisting of a small number of detector pixels is selected. The complete set of these windows covers a large part of SCIA-MACHY UV channel 1 (see Fig. 21). The wavelength microwindows are chosen in a way not to contain any atmospheric emission features that would perturb the Rayleigh information.

At lower wavelengths ($\leq$260 nm) the O_3 absorption in the Hartley-Huggins bands has a large impact on the radiative transfer. The ozone number density is contained as an additional retrieval species. However, very little information is contained in the mesospheric measurement. Thus no scientific benefit is gained from these results.

An MSIS profile (Hedin, 1991) is used as a priori for air density. The O_3 a priori profile has been obtained by extrapolation of mesospheric profiles measured by SCIAMACHY, see (Rohen, 2006).

4.1.2 Results

The retrieved profile of air density (Fig. 22) is in reasonable agreement with the model profile. The strong increase at altitudes above 85 km is due to straylight in SCIAMACHY's upper tangent heights (van Soest, 2006). However, the spectral data of SCIAMACHY have not been corrected for the pointing error yet. This offset accounts for values of up to 2 km (v. Savigny et al., 2005). That is, retrieved profiles might be shifted upwards by this value. Note that the offset between the model profile and the retrieved one is approximately 1.5 km. Note, however, there is no correlation yet between the choice of the a priori and the geolocation of the tangent point.

The averaging kernels as shown in Fig. 23 exhibit a FWHM of $\approx$5 km. This can be used as an estimate of the instrument's altitude resolution. The information content is near unity, indicating that the results are determined primarily by the measurement and not by the a priori. See Sect. 3.2.4 for a stringent derivation of averaging kernels.

Using support by mesospheric and thermospheric atmosphere models, possible applications for the retrieval of mesospheric air density contain retrievals of temperature as well as pressure. However, the retrieval results of air and O_3 are used primarily to have a good approximation of the background radiance, which is essential for the retrieval of
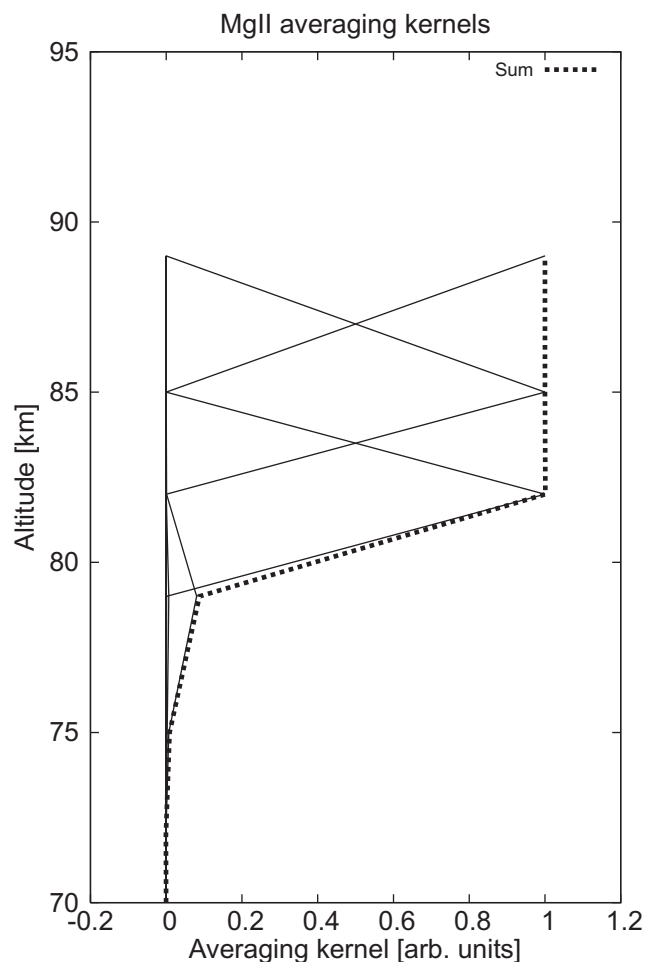

Fig. 28. Corresponding averaging kernels for Mg^+ (Fig. 27). The dashed line shows the sum of all kernels. As can be read from the averaging kernels, the information content of the measurement drops rapidly to zero for altitudes smaller than 82 km. The FWHM is approximately 5 km.

emission species. Thus, the results in terms of air density are not discussed in further detail here.

4.2 Mesospheric Mg and Mg^+

4.2.1 Retrieval setting

Mesospheric Mg and Mg^+ number densities are retrieved from emission features around 280 and 285 nm, respectively. These emission features are due to resonance fluorescence from the first excited states into the ground state (see Sect. 3.1.4 and Fig. 6). Mg^+ delivers two strong emission lines (279.553 nm, 280.270 nm), whereas only one strong neutral Mg line is observed (285.165 nm), see. Fig. 24.

The measured radiances are divided through by a solar spectrum of the same day measured by SCIAMACHY. A retrieval using the absolute radiances is possible in principle

but leads to very poor results compared to those using relative radiances.

4.2.2 Results

The Mg profile shows increased values at and above 85 km, see Fig. 25. This result is consistent with model calculations (Fritzenwallner and Kopp, 1998, Plane et al., 2003). These calculations suggest the maximum abundance of neutral Mg being located around 86–89 km and the peak concentration of Mg^+ located around 95–100 km (see Fig. 9a,b). However, it should be pointed out that the results from the SCIAMACHY measurements presented here do not prove the existence of a pronounced Mg layer around 87 km.

The profile of the ionized species Mg^+ is virtually zero below 85 km, though the limb signal is well pronounced (see Fig. 27). This indicates that the major abundance of ionized Magnesium is in located the thermosphere at altitudes above the top tangent altitude of SCIAMACHY. The thermospheric column densities agree well with LIDAR observations of the total column done over Wallops Island (36.9 N, $1.7 \cdot 10^{10}$ cm^{-2}) and Sardinia (36.2 N, $2.1 \cdot 10^{9}$ cm^{-2}) (comp. Fritzenwallner and Kopp, 1998).

As can be read from the averaging kernels shown in Figs. 26 and 28, the vertical resolution of the retrieval is approximately 5 km. The information content for Mg is well around 1 for altitudes above 75 km. Mg^+, however, performs worse. The measurement response drops rapidly to zero below 82 km.

5 Conclusions

The SCIAMACHY limb data exhibit a number of emission lines of metals species. These can be used to derive number densities on a global scale within the altitude range 65–92 km. Beside this, Rayleigh backscatter radiation can be utilized to derive mesospheric air number densities.

A forward model for radiative transfer calculations in the mesosphere has been developed. It has been coupled to an augmented Optimal Estimation Retrieval. Numerical improvements and stabilizations (such as preconditioning) have been applied.

A joint retrieval of Mg, Mg^+ and mesospheric air density is now available and has been tested. The retrieval has been optimized to the corresponding species by adaptive choice of spectral microwindows. The altitude resolution (5 km) at mesospheric altitudes is found to be worse than what can be expected from the actual limb tangent altitude step and FOV width (both approx 3 km). The pointing error of SCIAMACHY is not corrected for yet. It should be noted that the altitude profiles presented here are of preliminary nature.

Retrieval results of Mg, Mg^+ and air density show reasonable agreement with corresponding models. Column densities of the metallic species are in well agreement with previous rocket measurements. It should be noted, however, that the focus of this study was on the development an principal testing of the retrieval itself. The results for Mg and Mg^+ shown here do not justify any conclusions with respect to the global distribution and chemistry of neither metal species.

References

Anderson, J. G. and Barth, C. A.: Rocket Investigation of the MgI and MgII Dayglow, J. Geophys. Res., 76, 3723–3731, 1971.

Bovensmann, H., Burrows, J. P., Buchwitz, M., Frerick, J., Noel, S., and Rozanov, V. V.: SCIAMACHY: Mission Objectives and Measurement Modes, J. Atmos. Sci., 56, 127–150, 1999.

Burrows, J. P., Dehn, A., Deters, B., S., H., Richter, A., Voigt, S., and Orphal, J.: Atmospheric Remote–Sensing Reference Data from GOME: 2. Temperature–Dependent Absorption Cross Sections of O3 in the 231–794 nm range, Journal of Quantitative Spectroscopy and Radiative Transfer, 61, 509–517, 1999.

Chandrasekhar, S.: Radiative Transfer, Dover Publications Inc., New York, 1960.

Edlen, B.: The refractive index of air, Meteorologica, 2, 71–80, 1966.

Eichmann, K.-U.: Optimierung und Validierung des pseudosphischen Strahlungstransportmodells GOMETRAN, Master's thesis, University of Bremen, Institute of Environmental Physics, 1995.

Fritzenwallner, J. and Kopp, E.: Model Calculations of the Silicon and Magnesium Chemistry in the Mesosphere and Lower Thermosphere, Advances in Space Research, 21, 859–862, 1998.

Grebowsky, J. M., Pesnell, W. D., and Goldberg, R. A.: Do meteor showers significantly pertub the ionosphere?, Journal of Atmospheric and Solar-Terrestrial Physics, in press, 1998.

Hedin, A.: Extension of the MSIS Thermosphere Model into the Middle and Lower Atmosphere, J. Geophys. Res., 96, 1159, 1991.

Kaiser, J.: Atmospheric Parameter Retrieval from UV–Visible–NIR Limb Scattering Measurements, Ph.D. thesis, University of Bremen, Institute of Environmental Physics, 2001.

McNeil, W. J., Shu, T. L., and Murad, E.: Differential ablation of cosmic dust and implications for the relative abundances of atmospheric metals, J. Geophys. Res., 103, 10 899–10 911, 1998.

NIST: National Institute of Standards and Technology: Atomic Spectra Database, http://physics.nist.gov/PhysRefData/ASD/lines_form.html, 2005.

Noel, S., Bovensmann, H., Burrows, J. P., Frerick, J., Chance, K. V., and Goede, A. H. P.: Global Atmospheric Monitoring with SCIAMACHY, Physics and Chemistry of the Earth(C), 24, 427–434, 1999.

Plane, J. M. C.: Atmospheric Chemistry of Meteoric Metals, Chemical Reviews, 103, 4963–4984, 2003.

Plane, J. M. C. and Helmer, M.: Laboratory Study of the Reactions $Mg + O_3$ and $MgO + O_3$, Implications for the Chemistry of Magnesium in the Upper Atmosphere, Faraday Discussions, 100, 411–430, 1995.

Plane, J. M. C., Self, D. E., Vondrak, T., and Woodcock, K. R. I.: Laboratory studies and modelling of mesospheric iron chemistry, Advances in Space Research, 32, 699–708, 2003.

Roddy, P. A., Earle, G. D., Swenson, C. M., Carlson, C. G., and Bullett, T. W.: Relative concentrations of molecular and metallic ions in midlatitude intermediate and sporadic E–layers, Geophys. Res. Lett., 31, L19807, doi:10.1029/2004GL020604, 2004.

Rodgers, C. D.: Retrieval of atmospheric temperature and composition fom remote measurements of thermal radiation, Reviews of Geophysics and Space Physics, 14, 609–624, 1976.

Rohen, G. J.: Retrieval of upper stratospheric/lower mesospheric ozone profiles from SCIAMACHY limb scatter measurements and observations of the ozone depletion during the solar proton event in Oct./Nov. 2003, Ph.D. thesis, University of Bremen, Institute of Environmental Physics, 2006.

Rozanov, A.: Modeling of radiative transfer through a spherical planetary atmosphere, Ph.D. thesis, University of Bremen, Institute of Environmental Physics, 2001.

Scharringhausen, M.: Investigation of mesospheric and thermospheric magnesium species from space, Ph.D. thesis, University of Bremen, Institute of Environmental Physics, 2007.

Scharringhausen, M., Aikin, A., Burrows, J. P., and Sinnhuber, M.: Global column density retrievals of mesospheric and thermospheric MgI and MgII from SCIAMACHY limb and nadir radiance data, J. Geophys. Res., in press, 2008.

v. Savigny, C., Kaiser, J. W., Bovensmann, H., Burrows, J. P., McDermid, I. S., and Leblanc, T.: Spatial and temporal characterization of SCIAMACHY limb pointing errors during the first three years of the mission, Atmos. Chem. Phys., 5, 2593–2602, 2005, http://www.atmos-chem-phys.net/5/2593/2005/.

v. Savigny, C., Bramstedt, B., Noel, S., Sinnhuber, M., and Taha, G.: Comparison of SCIAMACHY pointing retrievals in limb and Occultation geometry, Tech. Rep. TN–IUP/IFE–2006–cvs–03, University of Bremen, Intitute of Environmental Physics, 2006.

van Soest, G.: Investigation of SCIAMACHY limb spatial straylight, Tech. Rep. SRON–EOS–RP–05–006, SRON, 2006.